2-1-2018

The Taurus Boundary of Stellar/Substellar (TBOSS) Survey. II. Disk Masses from ALMA Continuum Observations

Kimberly Ward-Duong
School of Earth and Space Exploration, kwardduong@smith.edu

J. Patience
School of Earth and Space Exploration

J. Bulger
National Institutes of Natural Sciences - National Astronomical Observatory of Japan

G. Van Der Plas
Universidad de Chile

F. Ménard
Université Grenoble Alpes

See next page for additional authors

Recommended Citation

Authors

Kimberly Ward-Duong, J. Patience, J. Bulger, G. Van Der Plas, F. Ménard, C. Pinte, A. P. Jackson, G. Bryden, N. J. Turner, P. Harvey, A. Hales, and R. J. De Rosa

The Taurus Boundary of Stellar/Substellar (TBOSS) Survey. II. Disk Masses from ALMA Continuum Observations

K. Ward-Duong[1] , J. Patience[1], J. Bulger[2,3] , G. van der Plas[4,5,6] , F. Ménard[6], C. Pinte[6] , A. P. Jackson[1,7] , G. Bryden[8],
N. J. Turner[8] , P. Harvey[9], A. Hales[10,11] , and R. J. De Rosa[12]

[1] School of Earth and Space Exploration, Arizona State University, P.O. Box 871404, Tempe, AZ 85287, USA; kwarduo@asu.edu
[2] Subaru Telescope, NAOJ, 650 N. Aohoku Place, Hilo, HI 96720, USA
[3] Institute for Astronomy Maui, University of Hawaii, 34 Ohia Ku Street, Pukalani, HI 96768, USA
[4] DAS, Universidad de Chile, Santiago, Chile
[5] Millennium Nucleus, "Protoplanetary Disks," El Observatorio 1515, Las Condes, Santiago, Chile
[6] Univ. Grenoble Alpes, Institut de Planétologie et d'Astrophysique de Grenoble (IPAG, UMR 5274), F-38000 Grenoble, France
[7] Centre for Planetary Sciences, University of Toronto, 1265 Military Trail, Toronto, ON M1C 1A4, Canada
[8] Jet Propulsion Laboratory, California Institute of Technology, 4800 Oak Grove Drive, Pasadena, CA 91109-8099, USA
[9] Univ. of Texas at Austin, Austin, TX 78712, USA
[10] Atacama Large Millimeter/Submillimeter Array, Joint ALMA Observatory, Alonso de Córdova 3107, Vitacura 763-0355, Santiago, Chile
[11] National Radio Astronomy Observatory, 520 Edgemont Road, Charlottesville, VA 22903-2475, USA
[12] Astronomy Department, University of California, Berkeley, CA 94720, USA
Received 2017 May 11; revised 2017 November 14; accepted 2017 November 26; published 2018 January 10

Abstract

We report 885 μm ALMA continuum flux densities for 24 Taurus members spanning the stellar/substellar boundary with spectral types from M4 to M7.75. Of the 24 systems, 22 are detected at levels ranging from 1.0 to 55.7 mJy. The two nondetections are transition disks, though other transition disks in the sample are detected. Converting ALMA continuum measurements to masses using standard scaling laws and radiative transfer modeling yields dust mass estimates ranging from ∼0.3 to 20 $M_\oplus$. The dust mass shows a declining trend with central object mass when combined with results from submillimeter surveys of more massive Taurus members. The substellar disks appear as part of a continuous sequence and not a distinct population. Compared to older Upper Sco members with similar masses across the substellar limit, the Taurus disks are brighter and more massive. Both Taurus and Upper Sco populations are consistent with an approximately linear relationship in $M_{\rm dust}$ to $M_{\rm star}$, although derived power-law slopes depend strongly upon choices of stellar evolutionary model and dust temperature relation. The median disk around early-M stars in Taurus contains a comparable amount of mass in small solids as the average amount of heavy elements in *Kepler* planetary systems on short-period orbits around M-dwarf stars, with an order of magnitude spread in disk dust mass about the median value. Assuming a gas-to-dust ratio of 100:1, only a small number of low-mass stars and brown dwarfs have a total disk mass amenable to giant planet formation, consistent with the low frequency of giant planets orbiting M dwarfs.

Key words: brown dwarfs – protoplanetary disks – stars: formation – stars: low-mass – stars: pre-main sequence

*Supporting material:* machine-readable table

1. Introduction

Submillimeter- and millimeter-wavelength observations of protoplanetary disks provide views into the disk structure, composition, evolution, and dust grain properties within the nascent environments of planet formation (see, e.g., Andrews & Williams 2005, 2007; Birnstiel et al. 2010; Ricci et al. 2010). Given assumptions regarding disk temperature and spatial extent and grain properties (e.g., opacity, emissivity, and size distribution), measurements of submillimeter/mm disk flux density can be translated into dust masses of grains with sizes similar to the observation wavelength (Beckwith et al. 1990).

By studying the properties of protoplanetary disks in star-forming regions with known ages, it is possible to use the abundance of dust and gas content within disks to trace disk evolution pathways and timescales. However, this is complicated by the dominant mode and scale of star formation, such as the environmental impacts of high-mass stellar populations, as within the Orion Molecular Cloud (OMC), or relatively quiescent low-mass environments, like the Taurus star-forming region. Measurements of disk evolution timescales and natal environments refine our understanding of formation mechanisms and provide context

for the history of the solar system, for which the meteoritic record and isotopic evidence offer important benchmarks on planetesimal growth timescales and indications of the Sun's formation environment (cf. MacPherson et al. 1995; Russell et al. 2006).

Previous surveys have examined stars with $M_* > 0.1\,M_\odot$ in a number of diverse star-forming regions, including Taurus (Andrews & Williams 2005; Andrews et al. 2013), IC 348 (Lee et al. 2011), Upper Sco (Mathews et al. 2012; Carpenter et al. 2014; Barenfeld et al. 2016; van der Plas et al. 2016), Lupus (Ansdell et al. 2016), σ Orionis (Ansdell et al. 2017), Chamaeleon I (Pascucci et al. 2016), and Orion (Williams et al. 2013; Eisner et al. 2016). In particular, great emphasis has been placed on the Taurus star-forming region given its proximity (∼140 pc) and canonically young age (∼1–2 Myr, although an older subpopulation may extend up to 20 Myr; Daemgen et al. 2015), which enable detailed studies of its stellar population. Surveys of Taurus have demonstrated a correlation of increasing disk mass with stellar mass (Andrews & Williams 2005; Andrews et al. 2013), suggesting that the mass of the disks in the Class II Taurus population ranges from ∼0.2% to 0.6% of the host mass. With comparisons to regions at the older age of Upper Sco, studies have also shown trends
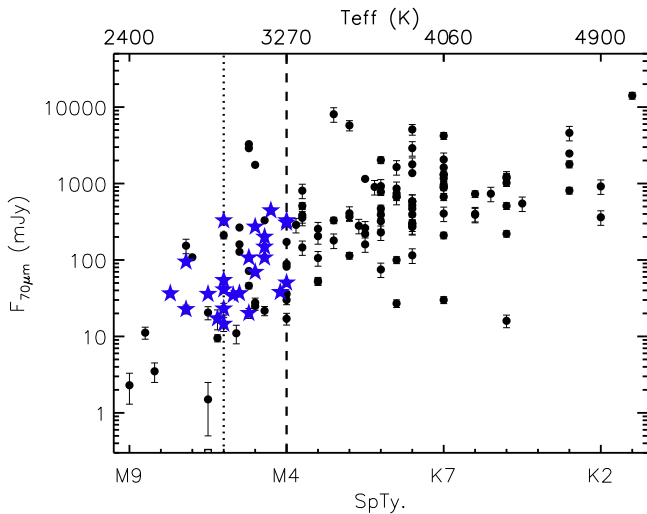
Figure 1. Flux at 70 μm from *Herschel* PACS or *Spitzer* MIPS observations of Taurus members as a function of spectral type. Only detections are plotted. The ALMA sample is indicated with blue stars. The dashed vertical line denotes the earliest M4 spectral type of the TBOSS sample, and the dotted line is the M6 spectral type near the stellar/substellar limit. The ALMA sample spans the range of 70 μm fluxes rather than being limited to the upper envelope of brightest sources.

of decreased dust mass for the same stellar masses at later ages (Carpenter et al. 2014; Barenfeld et al. 2016; van der Plas et al. 2016), and at mid-infrared wavelengths, disk studies of the low-mass stellar population with *Spitzer* revealed longer-lived excess emission for lower-mass stellar hosts (Carpenter et al. 2006).

With studies largely focusing on stars with masses >0.1 $M_\odot$, key questions remain as to whether similar disk-mass relations and depletion timescales hold for lower-mass stars and substellar objects. As the lowest-mass stars ultimately become the bulk of the stellar population by number—with M dwarfs comprising ~75% of the neighboring field population (Lépine 2005; Henry et al. 2006)—their disk properties represent what may be the most common pathways of planet formation. For the Taurus star-forming region that is the subject of this study, previous surveys (e.g., Andrews et al. 2013) have provided high detection rates around Class II solar-mass stars but few detections in the M-star range (0.1–0.6 $M_\odot$), and M-star disk detections are limited to the brightest subset of disks. To probe the full population of disks around low-mass stars and brown dwarfs in Taurus extending below the upper envelope of disk continuum emission, more sensitive observations are required and are the subject of this study. Furthermore, extending disk measurements across the hydrogen-burning limit is of significant interest, as relatively little is yet known about the planet populations of the lowest-mass stars and brown dwarfs. Recent transiting planet searches have revealed intriguing systems of low-mass planets orbiting M-dwarf hosts, including potentially temperate planets around Proxima Centauri (M5.5V, 0.12 $M_\odot$; Anglada-Escudé et al. 2016) and LHS1140 (M4.5V, 0.15 $M_\odot$; Dittmann et al. 2017) and the seven-planet system of TRAPPIST-1, an ultracool dwarf residing at the stellar/brown-dwarf boundary (M8V, 0.08 $M_\odot$; Gillon et al. 2017). To provide context for planet-hosting low-mass stars, investigations into protoplanetary disk hosts as younger analogs to systems like TRAPPIST-1 illustrate the early environments and physical processes

relevant to low-mass systems, allowing us to ascertain how their conditions impact the formation of planets.

To understand the diversity and evolution of planet-forming environments and to enable a comparison with the detected exoplanet population, comprehensive studies of disk properties require a wide range of stellar host masses, ages, and star-forming environments. Constraining disk properties for the full population therefore requires traversing the substellar boundary and necessitates sensitive observations in a lower-luminosity regime. Long-wavelength observations of the dust content within low-mass stellar and substellar disks have become viable with facilities such as the IRAM 30 m telescope, providing some of the initial explorations of brown-dwarf disks (Scholz et al. 2006). The large-program Submillimeter Array (SMA) survey by Andrews et al. (2013; with a 3σ sensitivity limit of 3 mJy) enabled disk detections for many higher-mass (>0.1 $M_\odot$) members of Taurus but few detections of the brightest low-mass stellar and brown-dwarf disks. Recently, studies using the Atacama Large Millimeter/submillimeter Array (ALMA) have enabled the measurement of disk properties for detected brown-dwarf disks in three systems in Taurus (Ricci et al. 2014), seven systems in Upper Sco (van der Plas et al. 2016), and 11 systems in ρ Ophiuchus (Testi et al. 2016), providing initial results regarding disk-mass deficits for these lower-mass hosts. With the sensitivity of ALMA for submillimeter/mm detections of brown-dwarf disks, large systematic surveys of disk populations bridging the gap across the substellar boundary are now possible.

In this paper, we present new ALMA Cycle 1 885 μm continuum observations of 24 low-mass stars and brown dwarfs in the Taurus star-forming region that were selected on the basis of previous *Herschel* detections at 70 and 160 μm (Bulger et al. 2014). In Section 2, we describe the sample and its selection from previous far-infrared Taurus surveys. Details of the ALMA observations and data reduction procedures are listed in Section 3. Section 4 provides the analysis methods to process the ALMA data and determine source flux densities, the results of which are given in Section 5. In Section 6, we describe the various methods used to estimate the dust masses of the disks and the central object masses of the host stars and discuss these relations in terms of the feasibility and timescale of planet formation. The summary and conclusions are given in Section 7.

2. Sample

The ALMA target sample consists of 24 Taurus low-mass stars and brown dwarfs with spectral types of M4–M7.75. The 24 targets represent a subset of *Herschel*-detected members from the 153-object Taurus Boundary of Stellar/Substellar (TBOSS) sample (Bulger et al. 2014) that is a 99% complete sample of M4–L0 Taurus members covering Class I–III objects. Class I and Class III detections from the TBOSS survey were not considered for the ALMA study. As shown in Figure 1, the observed targets span the full range of measured *Herschel* Photoconductor Array Camera and Spectrometer (PACS; Poglitsch et al. 2010) fluxes, so the sample is not biased to include only the brightest far-IR detections. Of the Class II M4–L0 members observed with *Herschel*, 75% were detected (Bulger et al. 2014),[13] making the *Herschel* detection criterion representative of the majority of the lowest-mass Class II Taurus objects. Table 1 lists the basic

---

[13] OT1_jpatienc_1.

Table 1
Sample Table

Target	Other Name	2MASS R.A. (J2000)	2MASS Decl. (J2000)	SpTy	F_{24} (mJy)	F_{70} (mJy)	F_{160} (mJy)	Notes	References
J04144730+2646264	FP Tau	04 14 47.309	+26 46 26.44	M4	143	307	351	Transition (homologously depleted)	(1)
J04555605+3036209	XEST 26–062	04 55 56.055	+30 36 20.96	M4	226	330	639	⋯	⋯
J05075496+2500156	CIDA 12	05 07 54.966	+25 00 15.61	M4	0	51	44	⋯	⋯
J04385859+2336351	⋯	04 38 58.599	+23 36 35.16	M4.25	20	38	76	⋯	⋯
J04190110+2819420	V410 X-ray 6	04 19 01.106	+28 19 42.05	M4.5	213	445	342	Transition (giant planet–forming)	(2)
J04161210+2756385	⋯	04 16 12.104	+27 56 38.58	M4.75	51	201	228	Transition	(3)
J04322210+1827426	MHO 6	04 32 22.109	+18 27 42.64	M4.75	20.7	107	188	Transition	(3)
J04334465+2615005	⋯	04 33 44.652	+26 15 00.53	M4.75	108	149	178	⋯	⋯
J04393364+2359212	⋯	04 39 33.645	+23 59 21.23	M5	59	70	44	⋯	⋯
J04394488+2601527	ITG 15	04 39 44.883	+26 01 52.79	M5	187	272	114	Binary: $\rho \sim 3''$	(4)
J04202555+2700355	⋯	04 20 25.554	+27 00 35.55	M5.25	25	107	100	Transition (primordial disk)	(1), (3)
J04284263+2714039	⋯	04 28 42.635	+27 14 03.91	M5.25	24	20	51	Transition, binary: $\rho \sim 0''63$	(2)
J04213459+2701388	⋯	04 21 34.599	+27 01 38.85	M5.5	9.6	37	101	Transition	(3)
J04181710+2828419	V410 Anon 13	04 18 17.106	+28 28 41.92	M5.75	28	35	<113	⋯	⋯
J04230607+2801194	⋯	04 23 06.073	+28 01 19.49	M6	19	41	38	⋯	⋯
J04262939+2624137	KPNO 3	04 26 29.392	+26 24 13.79	M6	12.9	23	33	⋯	⋯
J04292165+2701259	IRAS 04263+2654	04 29 21.653	+27 01 25.95	M6	310	329	176	Binary: $\rho \sim 0''2$	(5)
J04390163+2336029	⋯	04 39 01.631	+23 36 02.99	M6	22	15	<24	⋯	⋯
J04400067+2358211	⋯	04 40 00.676	+23 58 21.17	M6	20	55	52	⋯	⋯
J04141188+2811535	⋯	04 14 11.881	+28 11 53.51	M6.25	36	17	<293	Truncated	(3)
J04382134+2609137	GM Tau	04 38 21.340	+26 09 13.74	M6.5	53	36	<35	⋯	⋯
J04381486+2611399	⋯	04 38 14.861	+26 11 39.94	M7.25	73	95	67	⋯	⋯
J04390396+2544264	CFHT 6	04 39 03.960	+25 44 26.42	M7.25	18	23	<56	⋯	⋯
J04414825+2534304	⋯	04 41 48.250	+25 34 30.50	M7.75	21	37	<122	⋯	⋯

References. For transition disks and binary system identifications. (1) Currie & Sicilia-Aguilar (2011); (2) Cieza et al. (2012); (3) Bulger et al. (2014); (4) Itoh et al. (1999); (5) Konopacky et al. (2007).
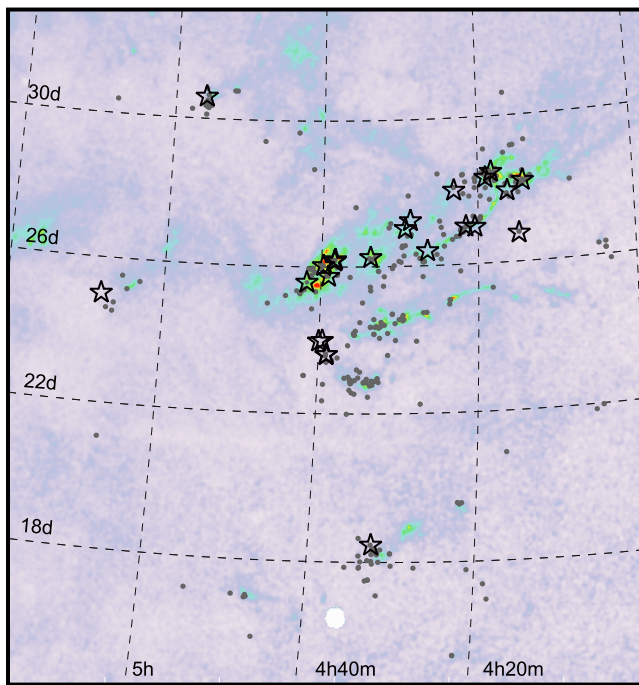
Figure 2. Spatial distribution of the ALMA sample (open stars) compared to the full TBOSS sample (Bulger et al. 2014; gray circles), overlaid on the extinction map from Dobashi et al. (2005). The ALMA sample covers many of the subregions in Taurus.

information for the ALMA Taurus targets, and the spatial distribution of the sample is mapped in Figure 2, along with the full TBOSS sample. While not a selection criterion, the sample includes seven examples of transition disks, as identified within previous mid-IR and submillimeter studies, and these targets and their corresponding references are identified in the notes of Table 1.

At the age of Taurus, a spectral type of M6.25 is the demarcation between stars and brown dwarfs (e.g., Luhman et al. 2005). All spectral types for this sample were determined spectroscopically and have a typical uncertainty of ±0.5 subclasses. Studies from the literature providing these spectral-type values are the following: Bulger et al. (2014), Briceño et al. (2002), Guieu et al. (2006), Kenyon & Hartmann (1995), Luhman & Rieke (1996), Luhman et al. (2006, 2009), Luhman (2004), Martín et al. (2001), Slesnick et al. (2006), and White & Basri (2003). There are 14 M4–M5 stellar and 10 M6–M7 substellar objects in the sample. Previous single-dish surveys (Andrews & Williams 2005; Scholz et al. 2006) have reported fewer M4–M5 submillimeter/mm detections than M6–M7 detections, and the sample is designed to characterize the transition from stellar to substellar disk properties with a sensitive ALMA survey.

3. Observations and Data Reduction

ALMA Band 7 observations were obtained for all targets in a series of tracks executed between 2013 November and 2014 July during the Cycle 1 Early Science campaign (program ID 2012.1.00743.S). Among the available ALMA bands, Band 7 represented the best compromise between declining disk flux with wavelength and increasing ALMA sensitivity with wavelength. For example, ALMA sensitivity is 1.7 times deeper at 1.2 mm than at 850 μm, but brown dwarfs with

detections at both wavelengths are ~2–4.5 times brighter at 850 μm compared to 1.2 mm (e.g., Bouy et al. 2008). The four spectral windows were centered on the following four frequencies: 331.8, 333.8, 343.8, and 345.7 GHz, providing a mean frequency of 338.8 GHz (885 μm). Since the central goal of the continuum survey was the detection of faint sources, the correlator was configured to the widest available setting of 2 GHz for three of the four spectral windows; the fourth spectral window centered on the highest frequency was configured in the only slightly narrower 1.875 GHz mode to enable a search for ^{12}CO(3–2) emission at a rest frequency of 345.70599 GHz. The aggregate sensitivity level across the full bandpass was set to reach an rms noise level of 0.15 mJy beam^{-1} to achieve an order of magnitude improvement over previous single-dish surveys. The continuum observations are the subject of this paper, while a companion paper is focused on the spectral channel observations (G. van der Plas et al. 2018, in preparation).

The 24 targets were divided into three ALMA scheduling blocks (SBs) based on science goals and proximity on the sky to ensure target positions within a 10° radius. Two SBs were observed twice ("Taurus2a" and "Taurus2b," consisting of targets of spectral type M5 and earlier), and one was observed three times ("Taurus1," consisting of targets of spectral type M6 and later), as listed in Table 2. The main observing sequence consisted of cycling through the Taurus sources and the gain/phase calibrators J0510+1800 and J0509+1806, depending on the observation. The phase calibrator J0509 +1806 was fainter than expected based on extrapolating archive fluxes from the SMA Observer Center[14] but was still sufficient for the data analysis. In addition to the observations of the phase calibrators every ~5–7 minutes, flux and bandpass calibrators were observed at the beginning of each track. Table 2 indicates which targets were allocated to each group, the observation dates, on-source time, range of baselines, and environmental and system conditions. The time on-source ranged from 5 to 10 minutes per target, and the precipitable water vapor (PWV) range of 0.36–1.13 mm corresponds to first–third octile conditions for ALMA.

4. Data Analysis

To convert raw ALMA observations into calibrated measurement sets, calibration and flagging tables derived from the ALMA quality-assurance process (Petry et al. 2014) were reapplied to the raw data in Common Astronomy Software Applications (CASA) 4.2.2 (McMullin et al. 2007). Minimal additional flagging was performed to remove data points that were identically zero and had been missed by the pipeline.

We adopted a uniform approach to continuum-imaging all of the targets within the three SBs in CASA. For each target, this included aligning the spectral windows between individual observations and concatenating the measurement sets, flagging all channels associated with CO emission as visually identified from plotting the amplitudes per channel, and averaging the remaining continuum channels after removing the CO-dominated channels.[15] Without flagging the CO channels, the median line flux for a target contributed ~1% additional emission over the full 7.875 GHz bandpass. Initial cleaned

---

[14] http://sma1.sma.hawaii.edu/callist/callist.html

[15] Example reduction scripts and auxiliary data are available at https://osf.io/9dyx4.

Group	Obs. UT Dates	Antennas	Time on Target (minutes)	Baseline Lengths (m)	Median PWV (mm)	Calibrators: Flux	Bandpass	Gain
Taurus1	2013 Nov 05	31	22:57	17.3–1300	0.91	J0238+166	J0423–0120	J0510+1800
	2013 Nov 05	31	31:18	17.3–1300	1.13	J0510+180	J0423–0120	J0510+1800
	2014 Jul 26	30	25:59	33.7–820.2	0.36	J0238+166	J0510+1800	J0510+1800
	Targets: J04141188, J04230607, J04262939, J04292165, J04381486, J04382134, J04390163, J04390396, J04400067, J04414825							
Taurus2a	2013 Nov 19	28	41:43	17.3–1300	0.58	J0510+180	J0423–0120	J0509+1806
	2014 Jul 27	33	20:47	24.2–820.2	0.5	J0510+180	J0510+1800	J0510+1800
	Targets: J04144730, J04161210, J04181710, J04190110, J04202555, J04213459, J04284263, J04322210							
Taurus2b	2013 Nov 17	29	18:45	17.3–1300	0.77	J0510+180	J0423–0120	J0509+1806
	2014 Jul 27	33	15:35	24.2–820.2	0.36	J0510+180	J0510+1800	J0510+1800
	Targets: J04334465, J04385859, J04393364, J04394488, J04555605, J05075496							

images were produced with natural weighting. From these images, 22/24 targets were detected, and the centers of continuum emission in the images were used to define new pointing centers, which were then applied to phase shift the measurement set of each target using the *visstat* CASA task. These new target coordinates are provided in Table 3, along with the offset from the 2MASS J2000 coordinates and proper motion values from Zacharias et al. (2015). The calibrated visibilities were then recleaned using natural, Briggs, and uniform weighting to compare the extracted flux values for each source. Average CLEAN beam sizes for the various weighting schemes were $0\rlap{.}''47 \times 0\rlap{.}''38$ (natural), $0\rlap{.}''33 \times 0\rlap{.}''22$ (uniform), and $0\rlap{.}''34 \times 0\rlap{.}''24$ (Briggs).

The *imfit* task in CASA was used to fit the continuum emission in the image plane with 2D Gaussians for each of the 22 detections. The phase-shifted measurement sets were also used to fit the continuum emission in the *uv* plane using the CASA task *uvmodelfit*, and the output source flux densities and uncertainties from the CASA tasks for each of the three weighting schemes in the image plane and *uvmodelfit* results are provided in Table 4. A comparison between the image-plane fitting and *uv* fitting for the extracted fluxes is shown in Figure 3. The extracted fluxes agree within 7% on average for all methods.

For the eight highest signal-to-noise ratio detections (S/N > 40), we also performed self-calibration, consisting of two or three rounds of phase-only self-calibration. The number of iterations was determined by repeating self-calibration until the source residual emission matched the rms noise level in the remainder of the field. For the self-calibrated sources, imaging was performed with Briggs weighting with "*robust*" = 0.5. For the remaining 16 sources with lower S/N, we adopt the fluxes obtained with natural weighting to maximize sensitivity in the image plane. The self-calibration or natural-weighting values from Table 4 are used for the subsequent analysis in the paper, and an additional 10% uncertainty was added to the uncertainties in Table 4 to account for the absolute flux scaling uncertainty; the ±10% absolute flux uncertainty dominates over the uncertainties from the measurements given in Table 4.

5. Results

Of the 24 Taurus low-mass stars and brown dwarfs observed with ALMA, a total of 21 targets are detected at $>8\sigma$ levels above the background, a much higher detection rate than previous submillimeter/mm brown-dwarf disk surveys with less sensitive instruments (e.g., Scholz et al. 2006). There is one marginal detection for J04141188 with S/N $\sim$ 3 in the cleaned image using Briggs weighting and S/N $\sim$ 5 in the cleaned image using natural weighting (this source was undetected with uniform weighting). Two sources—J04190110 (V410 X-ray 6) and J04213459—are not detected. The flux densities of the detections range from 1.0 to 55.7 mJy. The nondetections have 3σ upper limits of 0.27 mJy beam^{-1} for J04190110 and 0.29 mJy beam^{-1} for J04213459 based on the rms noise level in the map generated with natural weighting.

The ALMA 885 μm flux densities are plotted against the selection criterion of the *Herschel* 70 μm flux densities in Figure 4. Although the detection of 70 μm emission is well correlated with an ALMA 885 μm detection, there is approximately an order of magnitude scatter in the 885 μm flux density for a given 70 μm level. The two 885 μm upper limits are also not restricted to the faintest 70 μm sources. There is no qualitative distinction in the distributions of ALMA flux densities between the stellar M4–M5 and substellar M6–M7 populations. The transition disks identified by several studies (Currie & Sicilia-Aguilar 2011; Cieza et al. 2012; Bulger et al. 2014) are labeled in Figure 5. The transition disk flux densities from our ALMA study span the range of measured flux values for the full ALMA TBOSS sample, and they are not associated with lower 885 μm emission. Previous disk surveys have noted that transition disks can have bright submillimeter detections (e.g., Andrews et al. 2013; Ansdell et al. 2016).

The ALMA results form one of the largest sets of submillimeter detections of low-mass objects to date and define the lower boundary of the detected flux densities as a function of spectral type for Taurus. Figure 6 plots the Class II Taurus members with 850 or 890 μm detections. The faintest brown-dwarf disks are a factor of $\sim$500 dimmer than the brightest disks around early-K stars. Despite the

Table 3
Updated Target Positions from this Study and Proper Motions from Zacharias et al. (2015)

Target	J2000 Position (ALMA)	Offset from J2000 2MASS		$\mu_{\mathrm{R.A.}}$ mas yr^{-1}	$\mu_{\mathrm{Decl.}}$ mas yr^{-1}	Epoch
		R.A. (mas)	Decl. (mas)			
J04141188	04 14 11.8872 +028 11 52.8848	81.963	−625.2	8 ± 5.3	−26.7 ± 5.3	2013.310
J04144730	04 14 47.3215 +026 46 26.1018	167.398	−338.2	5.1 ± 5.2	−21.6 ± 5.2	2013.424
J04161210	04 16 12.1253 +027 56 38.1025	282.248	−477.5	11 ± 5.2	−29.5 ± 5.2	2013.341
J04181710	04 18 17.1158 +028 28 41.6474	129.213	−272.6	4.7 ± 5.5	−19.7 ± 5.5	2013.108
J04202555	04 20 25.5760 +027 00 35.2819	294.006	−268.1	14.3 ± 5.3	−19.6 ± 5.3	2013.395
J04230607	04 23 06.0891 +028 01 19.1665	213.188	−323.5	13.4 ± 5.2	−23.2 ± 5.2	2013.335
J04262939	04 26 29.4038 +026 24 13.4991	158.536	−290.9	9.3 ± 5.3	−20.4 ± 5.3	2013.248
J04284263	04 28 42.6452 +027 14 03.3013	136.039	−608.7	−5.1 ± 5.2	−11.7 ± 5.2	2013.326
J04292165	04 29 21.6580 +027 01 25.5845	66.811	−365.5	5.5 ± 5.2	−22.7 ± 5.2	2013.342
J04322210	04 32 22.1273 +018 27 42.4070	260.373	−233	13.8 ± 6.3	−16.8 ± 6.3	2013.571
J04334465	04 33 44.6685 +026 15 00.1949	221.976	−335.1	11.2 ± 5.2	−17.3 ± 5.2	2013.499
J04381486	04 38 14.8866 +026 11 39.6288	344.564	−311.2	7.8 ± 10	−17.8 ± 10	2013.856
J04382134	04 38 21.3433 +026 09 13.4528	44.432	−287.2	2.1 ± 5.6	−12.8 ± 5.6	2013.309
J04385859	04 38 58.6108 +023 36 34.8674	162.184	−292.6	11.5 ± 5.5	−19.8 ± 5.5	2013.572
J04390163	04 39 01.6425 +023 36 02.6857	158.072	−304.3	10.7 ± 5.4	−21.2 ± 5.4	2013.681
J04390396	04 39 03.9673 +025 44 26.1032	98.634	−316.8	4.7 ± 5.5	−19.9 ± 5.5	2013.598
J04393364	04 39 33.6491 +023 59 20.9331	56.188	−296.9	4.3 ± 5.4	−20.1 ± 5.4	2013.831
J04394488	04 39 44.8920 +026 01 52.3806	121.305	−409.4	2.9 ± 5.5	−21 ± 5.5	2013.518
J04400067	04 40 00.6799 +023 58 20.7921	53.454	−377.9	3.2 ± 5.5	−23.5 ± 5.5	2013.579
J04414825	04 41 48.2591 +025 34 30.2815	123.126	−218.5	−1.8 ± 6	−9.7 ± 6	2013.737
J04555605	04 55 56.0714 +030 36 20.4410	211.73	−519	6.3 ± 5.1	−30.5 ± 5.1	2013.739
J05075496	05 07 54.9702 +025 00 15.3837	57.095	−226.3	2.3 ± 5.1	−13.3 ± 5.1	2013.609

Table 4
Measured Flux Density Values for the 24 Targets in this Sample, with the Spectral Types and Corresponding Estimated Effective Temperatures, Luminosities, and Masses for the Central Objects

| Target	SpTy	T_{eff} (K)	$\log L_*$ ($L_\odot$)	M_*(B15) ($M_\odot$)	Natural Weighting Flux (mJy)	Briggs Weighting Flux (mJy)	Uniform Weighting Flux (mJy)	uvmodelfit[a] Flux (mJy)	Note
J04292165	M6	2858	−1.566	0.058	7.35 ± 0.19	7.21 ± 0.34	6.98 ± 0.38	7.28 ± 0.22	⋯
J04141188	M6.25	2836	−1.628	0.053	1.06 ± 0.21	0.71 ± 0.20	⩽0.55	1.25 ± 0.30	⋯
J04230607	M6	2858	−1.566	0.058	5.94 ± 0.24	5.68 ± 0.35	5.7 ± 0.4	6.36 ± 0.23	⋯
J04262939	M6	2858	−1.566	0.058	5.4 ± 0.13	5.7 ± 0.22	5.58 ± 0.25	5.61 ± 0.15	⋯
J04381486	M7.25	2747	−1.881	0.035	1.36 ± 0.11	1.66 ± 0.24	1.62 ± 0.30	1.57 ± 0.16	⋯
J04382134	M6.5	2814	−1.689	0.048	2.8 ± 0.12	2.62 ± 0.18	2.62 ± 0.21	2.75 ± 0.15	⋯
J04390163	M6	2858	−1.566	0.058	1.3 ± 0.16	1.13 ± 0.26	1.48 ± 0.59	1.73 ± 0.26	⋯
J04390396	M7.25	2747	−1.881	0.035	2.46 ± 0.13	2.33 ± 0.21	2.23 ± 0.23	2.28 ± 0.15	⋯
J04400067	M6	2858	−1.566	0.058	9.74 ± 0.25	7.81 ± 0.21	7.84 ± 0.23	7.93 ± 0.15	SC
J04414825	M7.75	2696	−2.02	0.028	3.41 ± 0.14	3.34 ± 0.22	3.45 ± 0.26	3.52 ± 0.16	⋯
J04144730	M4	3191	−0.701	0.199	18.68 ± 0.26	15.03 ± 0.50	15.05 ± 0.58	14.96 ± 0.19	SC
J04161210	M4.75	3027	−0.959	0.135	5.71 ± 0.17	5.47 ± 0.30	5.38 ± 0.38	5.84 ± 0.19	⋯
J04181710	M5.75	2883	−1.488	0.053	1.35 ± 0.16	1.18 ± 0.21	1.14 ± 0.24	1.51 ± 0.19	⋯
J04202555	M5.25	2943	−1.15	0.101	18.31 ± 0.27	14.43 ± 0.40	14.21 ± 0.44	15.32 ± 0.19	SC
J04284263	M5.25	2943	−1.15	0.101	1.53 ± 0.14	1.67 ± 0.24	1.76 ± 0.31	1.89 ± 0.23	⋯
J04322210	M4.75	3027	−0.959	0.135	55.65 ± 0.54	48.28 ± 0.75	48.4 ± 0.85	47.77 ± 0.23	SC
J04334465	M4.75	3027	−0.959	0.135	40.25 ± 0.37	35.18 ± 0.68	35.18 ± 0.71	36.33 ± 0.23	SC
J04385859	M4.25	3133	−0.777	0.177	30.00 ± 0.30	26.75 ± 0.45	26.56 ± 0.49	28.29 ± 0.22	SC
J04393364	M5	2982	−1.056	0.117	9.46 ± 0.25	8.09 ± 0.23	8.19 ± 0.27	7.97 ± 0.16	SC
J04394488	M5	2982	−1.056	0.117	11.26 ± 0.27	9.01 ± 0.25	8.7 ± 0.26	9.44 ± 0.16	SC
J04555605	M4	3191	−0.701	0.199	1.01 ± 0.10	1.61 ± 0.36	1.66 ± 0.51	1.47 ± 0.15	⋯
J05075496	M4	3191	−0.701	0.199	2.88 ± 0.12	2.9 ± 0.23	2.93 ± 0.28	3.06 ± 0.17	⋯
J04213459	M5.5	2911	−1.236	0.088	⩽0.29	⩽0.41	⩽0.48	⋯	Non-Det.
J04190110	M4.5	3078	−0.864	0.155	⩽0.27	⩽0.39	⩽0.47	⋯	Non-Det.

Note. SC corresponds to sources for which self-calibration has been performed, and upper limits denote 3× the rms in the residual image.
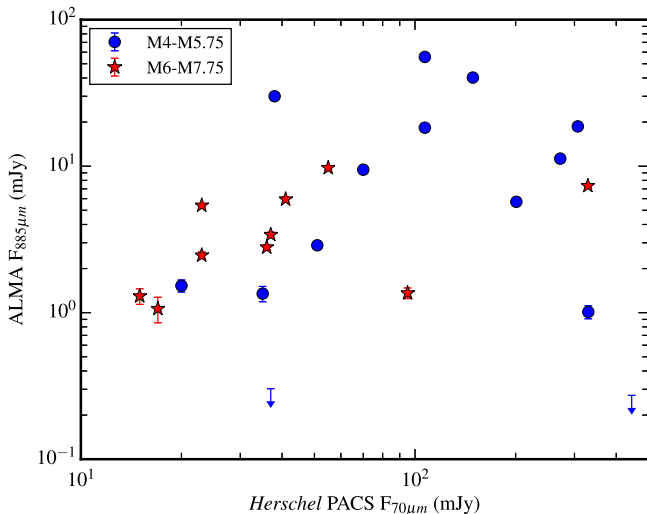[a] The typical reduced χ^2 value for the fit is ∼1.45.

large difference in the typical level of emission, both the earlier and later spectral types exhibit a considerable dispersion of at least a factor of 10 about the average value. This large dispersion appears to be a universal characteristic of disk populations and is seen in surveys of a number of other regions, such as Upper Sco (Barenfeld et al. 2016), Lupus (Ansdell et al. 2016), and Cha I (Pascucci et al. 2016).
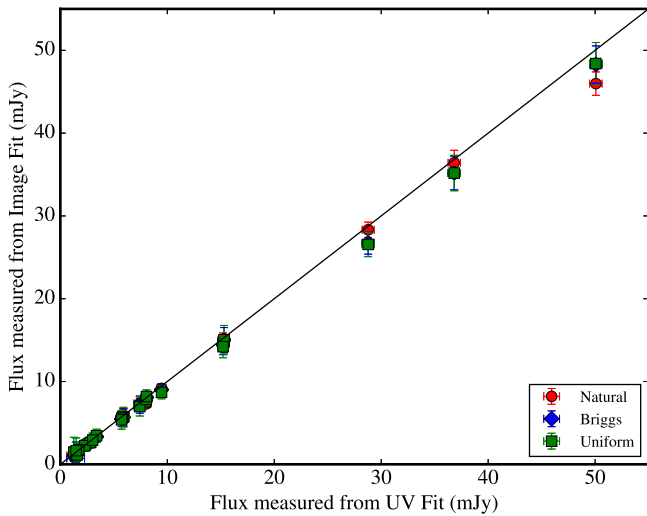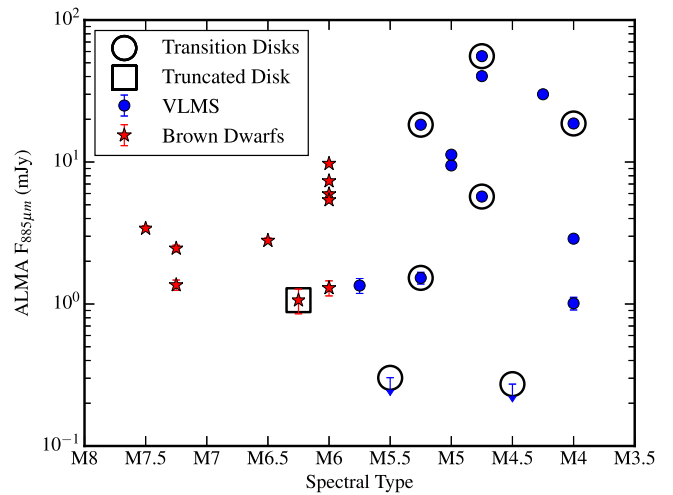
Figure 3. Flux density derived from the CASA *imfit* routine applied to the non–self-calibrated continuum maps generated with different weighting schemes (natural, red; Briggs, blue; uniform, green) as a function of the flux density derived from the CASA *uvmodelfit* routine applied to visibilities. Error bars shown are 3σ uncertainties. The results are consistent, with an average difference of 7%.
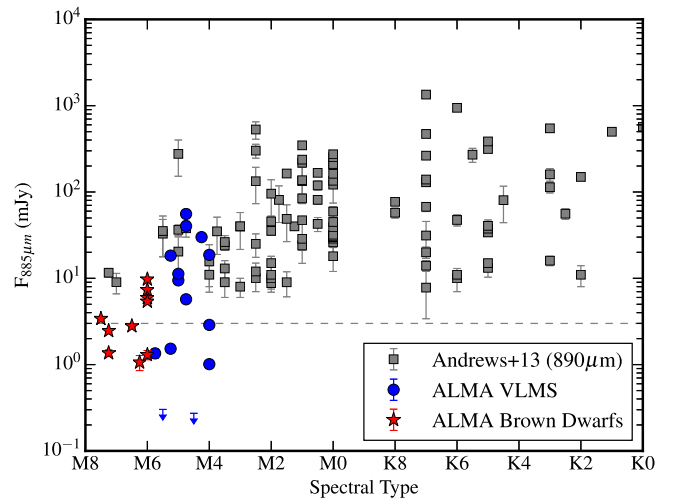

Figure 5. New ALMA 885 μm fluxes from the 24 targets in our study. All but two of the targets have continuum detections, and the two nondetections are both transition disks. However, additional transition disks (circled) are also found within the very-low-mass star (VLMS) population within our sample, and a single truncated disk (square) was identified for one of the brown dwarfs in our sample.

Figure 4. Measurements and upper limits at 885 μm from ALMA as a function of *Herschel* measurements at 70 μm for each source in the sample. The M4–M5.75 subset is shown as blue circles, and the M6–M7 subset is plotted as red stars.

Figure 6. New ALMA 885 μm fluxes from the 24 targets in our study (red stars and blue circles) as a function of spectral type, shown with a previous compilation of measured or extrapolated 890 μm fluxes for Class II Taurus members from Andrews et al. (2013; gray squares), with the survey sensitivity limit shown for comparison (gray dashed line).

Among the ALMA-observed TBOSS targets in this sample, three are known binaries (Itoh et al. 1999; Konopacky et al. 2007; Kraus et al. 2012), two were previously identified as binary candidates (Kraus et al. 2012), and a target within our sample also shows an 885 μm detection from a secondary source unassociated with any previously identified companions or candidates. Separations of the components are listed in Table 5. For the binary with a separation less than the beam size—J04292165—the continuum emission detection cannot be divided into primary and secondary disks, though the emission appears slightly extended and follow-up higher resolution mapping would determine the relative contributions from each component of the binary system. The total flux density is reported in Table 4 for this system. Two targets—

J04284263 and J04394488—are binaries with separations greater than the beam size. The subarcsecond pair J04284263 is not spatially resolved in the ALMA map in Figure 7, while the $\sim$3″ pair J04394488 exhibits clear emission from both components. For the system J04181710, a secondary source 9″6 in separation from the target was detected at 3σ; however, a corresponding source has not been previously reported in the literature for this target, making the background or associated nature of the source uncertain. For both the known binary and new candidate detections, the secondary disks are weaker in both cases, and the lower flux densities are reported in Table 5. An additional two targets—J04202555 and J04230607—were previously noted as binary candidates with separations ⩽4″6 (Kraus et al. 2012). Neither of these candidates are detected in

Table 5
Binary Companion Candidates and Their Corresponding ALMA
Measurements within This Study

System	Candidate Flux (mJy)	Sep. (arcsec)	Pos. Ang. (deg)	References
J04181710	0.99 ± 0.16	9.6	77.6	(1)
J04394488	1.61 ± 0.18	3.1	324.8	(1), (2)
J04202555	$\leqslant 0.42$	4.62	267.6	(3)
J04230607	$\leqslant 0.42$	6.44	291.6	(3)
J04284263	*	0.64	10	(4)
J04292165	*	0.22	268.6	(5)

Note. Candidates denoted by * are not spatially resolved in the ALMA maps.
References. (1) This work; (2) Itoh et al. (1999); (3) Kraus et al. (2012); (4) Cieza et al. (2012); (5) Konopacky et al. (2007).

the wider field maps in this study, and the 3σ upper limits at the positions of the candidates are included in Table 5.

By combining the new 885 μm data with previously reported photometry from the literature (compiled in mJy with original references in Bulger et al. 2014), the spectral energy distribution (SED) for each source was constructed. Each source SED is presented for stellar objects (M4–M5.75) in Figure 7 and for substellar objects (M6 and later) in Figure 8, along with the associated ALMA continuum map. For many of the targets, the ALMA flux density is the only detection in the submillimeter/mm wavelength range critical for estimating disk masses.

6. Discussion

6.1. Calculations of Disk Masses from Analytic Relations

The Taurus target flux densities reported in Table 4 are converted into estimates of the disk dust mass through two approaches: (1) applying flux-mass scaling relations and (2) fitting radiative transfer models to the SEDs, including the new ALMA 885 μm values. For this analysis, the natural-weighting map fluxes are used for consistency; however, the results are not dependent on the procedure applied to determine fluxes as shown in Figure 3. The analytic expression utilized to estimate disk masses is

$$\log M_{\rm dust} = \log S_\nu + 2\log d - \log \kappa_\nu - \log B_\nu(\langle T_{\rm dust}\rangle), \quad (1)$$

where S_ν is the ALMA flux density, d is the distance, κ_ν is the dust opacity, and $B_\nu(\langle T_{\rm dust}\rangle)$ is the blackbody function at the dust temperature (Hildebrand 1983).

The first three terms of Equation (1) are determined directly from measurements or standard assumptions. The ALMA flux S_ν for each source is given by the natural-weighting or self-calibration value in Table 4. A distance to Taurus of 140 pc (Kenyon et al. 1994; Bertout et al. 1999; Torres et al. 2009) is used in the calculation. The opacity was scaled to the observation wavelength of 885 μm from the assumptions of $\kappa_{\rm 1.3mm} = 2.3$ cm^2 g^{-1} and $\kappa \sim \nu^{0.4}$; this opacity normalization value and power-law relation correspond to the opacity of a standard mixture of astronomical silicates with a maximum grain size $a_{\rm max} = 1$ mm and a grain size distribution following a power law with slope $= -3.5$, similar to previous studies (Andrews et al. 2013; Carpenter et al. 2014).

Different approaches have been used in the literature to estimate the value of $T_{\rm dust}$ needed for the final term of Equation (1). A fixed temperature, typically $\sim$20 K, has been

applied to early work on Taurus (Beckwith et al. 1990) and recent ALMA surveys of Lupus and Cha I (Ansdell et al. 2016; Pascucci et al. 2016). A temperature-scaling relation based on object luminosity was introduced and applied to surveys of more massive stars in Taurus and Ophiuchus (e.g., Andrews et al. 2013):

$$\langle T_{\rm dust}\rangle = 25(L_*/L_\odot)^{1/4} K. \quad (2)$$

To estimate the luminosity required for Equation (2), measurements of the object photosphere, such as a spectrum or photometric SED, are compared with evolutionary models. For this study, we determine the target luminosities given in Table 4 from a scaling relation of spectral type with effective temperature, and evolutionary models assuming a fixed age for Taurus, and the procedure is described in further detail in Section 6.3 and Appendix A. For low-luminosity objects such as the targets in this study, the dust scaling given in Equation (2) predicts very low $T_{\rm dust}$ values, with average values of 12 K, comparable to the ambient molecular cloud. The values of $T_{\rm dust}$ from Equation (2) and the corresponding $M_{\rm dust}$ are reported in Appendix D.

To avoid the unphysically low temperatures implied by Equation (2), a different temperature–luminosity relation more appropriate for samples extending to spectral types of $\sim$M5 and later was used, as explored in our previous paper (van der Plas et al. 2016):

$$\langle T_{\rm dust}\rangle = A(L_*/L_\odot)^B K. \quad (3)$$

Both the normalization factor A and power-law index B in Equation (3) vary depending on a number of factors, with the assumed outer radius of the disk being the dominant parameter; the coefficients A and B for different outer radii are reported in Table 6. For the subsequent analysis in the paper, the analytic estimate of the disk dust mass is based on Equation (3), and we explore a range of radii from 10 to 200 au. The full range of $T_{\rm dust}$ and $M_{\rm dust}$ for each target assuming different radii is given in Appendix D, and a subset of values are listed in Table 7. As expected, the differences are most pronounced for the lowest-luminosity objects, with variations in dust mass of $\sim$2.5$\times$ between the 40 and 200 au disks. To account for a range of possible disk sizes, the $M_{\rm dust}$ uncertainties incorporate both the $\pm$10% flux scaling and sizes of $\pm$tens of au about a central disk size; we explore cases with central disk sizes of 100 au for all objects (used in previous studies) and cases with central disk sizes of 40 or 20 au for the lower-mass objects and 100 au for the higher-mass objects.

6.2. Calculations of Disk Masses from Radiative Transfer Models (MCFOST)

The final approach to determining disk masses from the ALMA measurements involves a combination of the ALMA data with photometry at other wavelengths and a comparison with models generated with the Monte Carlo 3D continuum radiative transfer code MCFOST (Pinte et al. 2006, 2009), which produces synthetic SEDs. In the MCFOST routines, photons from the central object are propagated through the disk with a model incorporating a combination of scattering, absorption, and reemission. The MCFOST parameters related to the central source are the central object effective temperature $T_{\rm eff}$, object radius R, and luminosity L_*. These values are listed for each source in Table 8, where the stellar radius and value of A_v for each source were derived with SED fitting in the
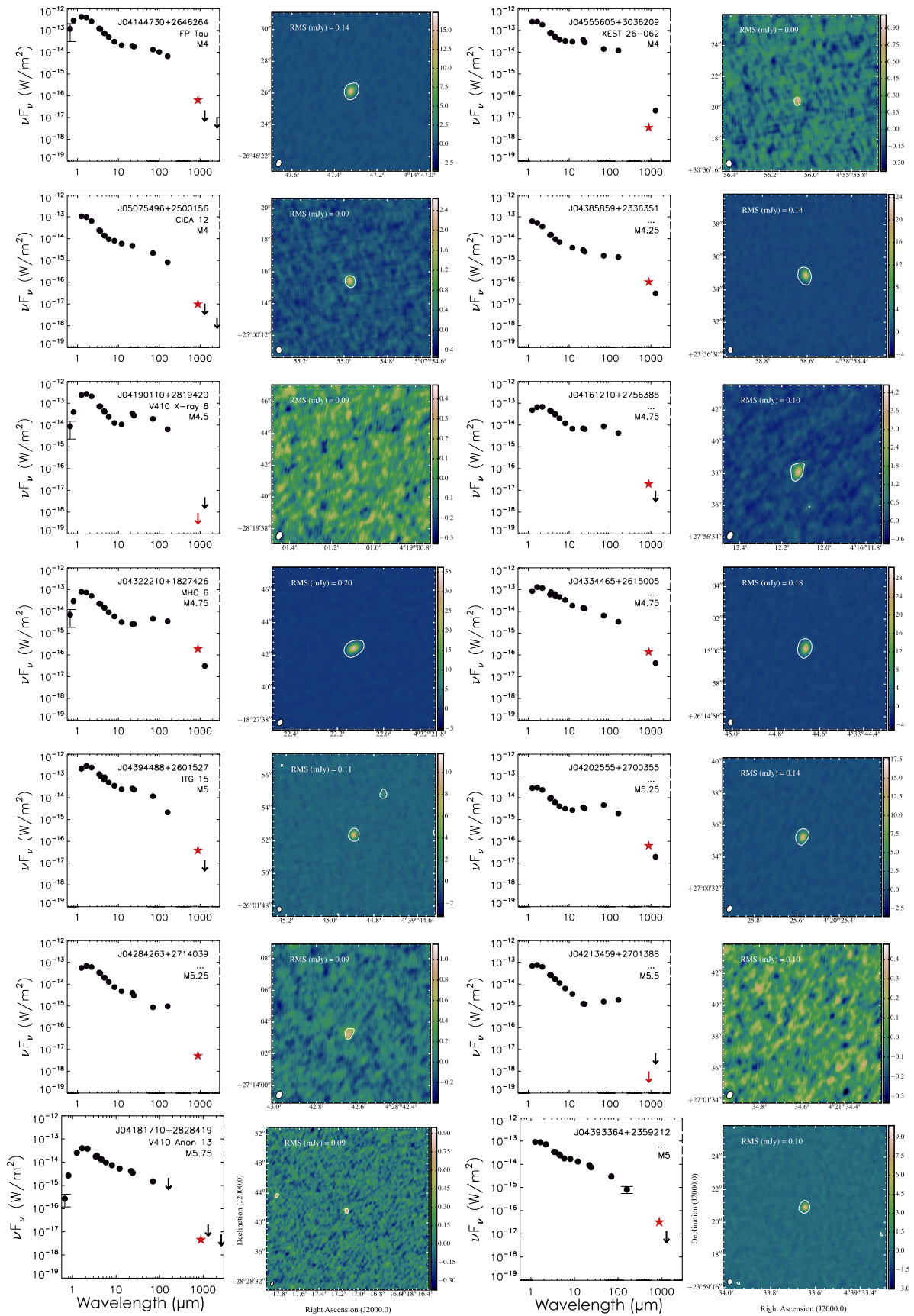
Figure 7. SEDs and continuum maps for targets with spectral types M4–M5.75. Map intensity corresponds to flux density in mJy. All contours shown are 5σ. For J04181710, the field of view has been increased to show a wide companion candidate detection. Beam sizes are indicated in the lower left corner with white ellipses, with typical sizes of 0″.47 × 0″.38.
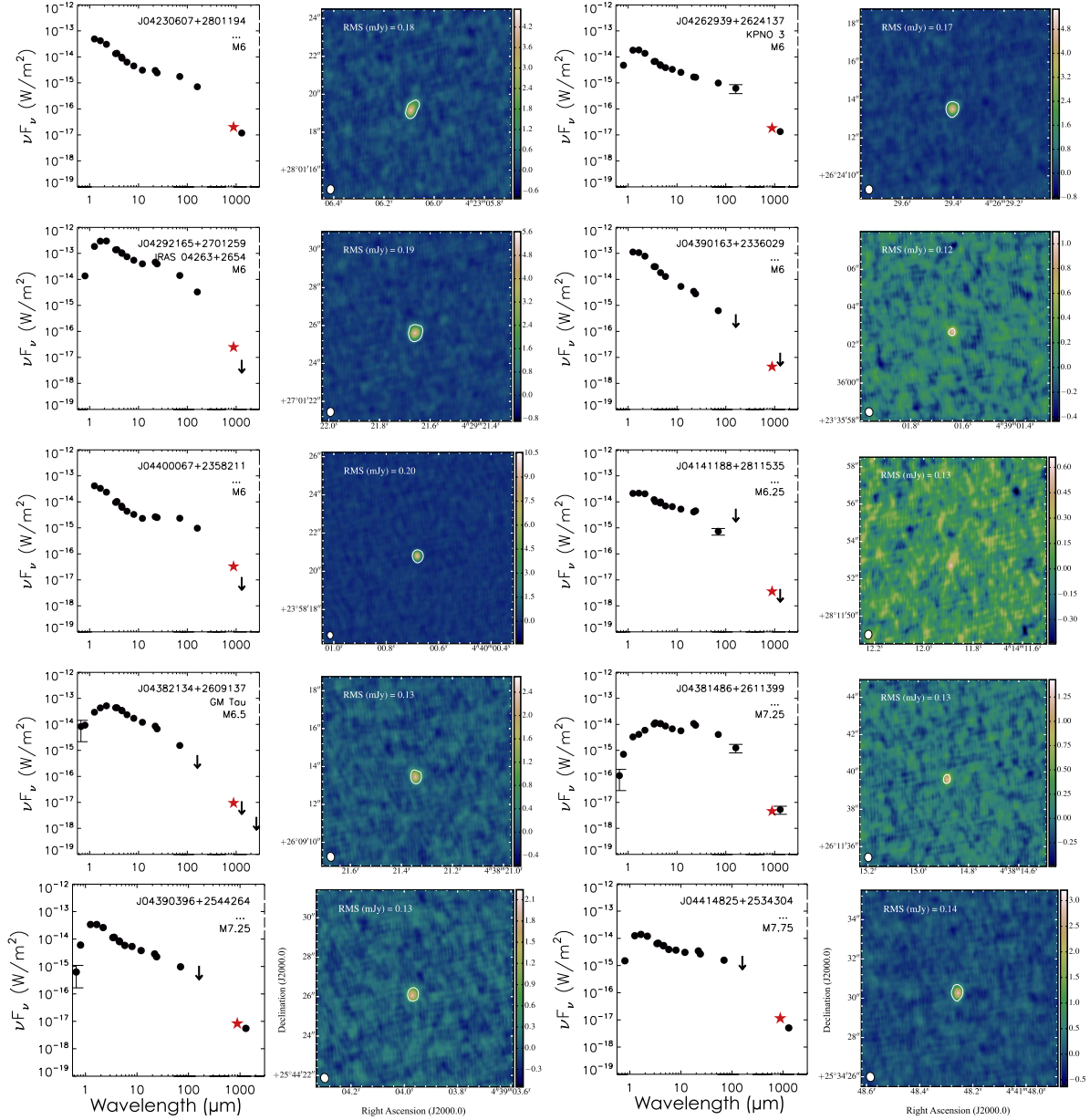
Figure 8. SEDs and ALMA continuum maps for targets with spectral types M6 and later. Map intensity corresponds to flux density in mJy. All contours are 5σ. Beam sizes are indicated with white ellipses in the lower left corner, with typical sizes of $0\farcs47 \times 0\farcs38$.

Table 6
1 Myr Disk Dust Temperature Power-law Coefficients for Low-luminosity Central Objects (Typically $L < 0.1\ L_\odot$), from the Relations Provided in van der Plas et al. (2016)

$T_{\rm dust} = A(L_*/L_\odot)^B$		
Disk Outer Radius (au)	Amplitude (A)	Index (B)
10	58	0.23
20	41	0.22
40	30	0.18
60	26	0.16
80	24	0.15
100	22	0.15
200	19	0.14

previous *Herschel* TBOSS study by Bulger et al. (2014). The effective temperatures were estimated from the spectroscopically determined spectral types reported in the literature (references in Table 1) and the temperature scales from Luhman et al. (2005) and Kenyon & Hartmann (1995). A set of nine parameters is used to define a disk structure and dust population: dust mass $M_{\rm dust}$, inner radius $r_{\rm in}$, outer radius $r_{\rm out} = 100$ au, scale height H_0 at a reference radius r_o, flaring profile exponent β for the disk height $H(r) \sim r^\beta$, surface density profile index b where $\Sigma(r) \sim r^b$, minimum grain size $a_{\rm min} = 0.01\ \mu$m, maximum grain size $a_{\rm max} = 3$ mm, and grain size distribution $N(a) \sim a^{-3.5}$ with a corresponding continuum opacity $\kappa = 2.78\ {\rm cm}^2/{\rm g}$ at $870\ \mu$m; five of these are varied over ranges reported in Table 9. The final parameters are the disk inclination i and the reddening $A_{\rm v}$. Since none of the

Table 7
Dust Masses

Target	$R = 40$ au		$R = 100$ au		$R = 200$ au	
	T_d (K)	$M_d(\oplus)$	T_d (K)	$M_d(\oplus)$	T_d (K)	$M_d(\oplus)$
J04292165	15.7	2.72	12.8	3.82	11.5	4.67
J04141188	15.3	0.41	12.5	0.57	11.2	0.70
J04230607	15.7	2.20	12.8	3.09	11.5	3.78
J04262939	15.7	2.00	12.8	2.81	11.5	3.43
J04381486	13.8	0.63	11.5	0.86	10.4	1.05
J04382134	14.9	1.12	12.3	1.57	11.0	1.92
J04390163	15.7	0.48	12.8	0.67	11.5	0.83
J04390396	13.8	1.13	11.5	1.56	10.4	1.90
J04400067	15.7	3.61	12.8	5.06	11.5	6.19
J04414825	13.0	1.73	11.0	2.36	9.9	2.88
J04144730	22.4	4.04	17.3	5.94	15.2	7.30
J04161210	20.2	1.44	15.8	2.09	13.9	2.56
J04181710	16.2	0.47	13.2	0.67	11.8	0.82
J04202555	18.6	5.18	14.8	7.45	13.1	9.13
J04284263	18.6	0.43	14.8	0.62	13.1	0.76
J04322210	20.2	14.02	15.8	20.35	13.9	24.98
J04334465	20.2	10.14	15.8	14.72	13.9	18.07
J04385859	21.7	6.78	16.8	9.93	14.8	12.21
J04393364	19.4	2.53	15.3	3.65	13.5	4.48
J04394488	19.4	3.01	15.3	4.35	13.5	5.33
J04555605	22.4	0.22	17.3	0.32	15.2	0.40
J05075496	22.4	0.62	17.3	0.92	15.2	1.13

Table 8
Stellar Parameters Used in MCFOST Models

Target	$T_{\rm eff}$ (K)	$\log[L_*]$ ($L_\odot$)	R_* ($R_\odot$)	A_v (mag)
J04141188	2963	−1.746	0.873	2.5
J04144730	3270	−0.49	1.734	0.7
J04161210	3162	−1.084	1.385	2
J04181710	3023	−0.987	0.422	2.8
J04190110	3058	−0.454	0.589	1.1
J04202555	3091	−1.343	0.487	1.6
J04213459	3058	−0.912	1.136	0.9
J04230607	2990	−1.332	0.942	1.5
J04262939	2990	−1.655	0.377	1.6
J04284263	3091	−1.258	1.217	1.3
J04292165	3091	−0.115	1.884	0.4
J04322210	3162	−1.134	1.385	1.4
J04334465	3162	−0.565	0.554	3.0
J04381486	2837	−2.358	0.579	1.0
J04382134	2935	−1.507	0.794	0.6
J04385859	3234	−1.148	0.622	1.5
J04390163	2990	−1.054	1.13	0.5
J04390396	2837	−1.336	0.552	0.5
J04393364	3125	−1.031	1.300	1.0
J04394488	3125	−0.295	2.600	0.5
J04400067	2990	−1.547	0.377	0.5
J04414825	2752	−1.683	0.634	1.3
J04555605	3270	−0.576	1.652	0.0
J05075496	3270	−1.095	1.652	1.2

Table 9
MCFOST Model Parameter Ranges

Parameter	Minimum	Maximum
Disk mass, $M_{\rm dust}$	10^{-8}	10^{-4}
Scale height, H_0	5	25
Inner radius, $r_{\rm in}$	0.01	1.0
Disk flaring index, β	1.0	1.3
Surface density index	−1.5	0.0

objects are in the more embedded Class I phase, a single continuous disk model was used, with no envelope component.

We apply a genetic algorithm approach, previously employed in Mathews et al. (2013), to explore five free model parameters: $M_{\rm dust}$, H_0, $r_{\rm in}$, β, and surface density index. These parameters are iteratively varied over a range of values to construct a minimal χ^2 distribution. For each target, the genetic algorithm begins with an initial generation of models uniformly sampled over the free-parameter minimum and maximum ranges given in Table 9 and calculates χ^2 values for each model. A successive generation of models is then generated by selecting from the previous generation of parent models, with parameters randomly sampled from the parent-model parameters. Within the successive generation, a "mutated" subset of models is created by varying one-tenth of the parent parameter ranges for a fraction of models. The process is continued for following generations, with the range of parameter variation and mutation rate dependent upon the resulting χ^2 values, optimizing to more densely sample the parameter space near the minimum of the distribution. The best-fit parameter values corresponding to the minimum χ^2 for each SED fit are listed in Table 10, and the dust masses are compared with the analytically derived masses in Figure 9. The SEDs with the resulting best-fit MCFOST models are provided in Appendix C for each of the stellar and brown-dwarf targets (Figures 31 and 32, respectively).

6.3. Disk Mass as a Function of Central Object Mass

The disk masses determined from the new ALMA data represent the lowest-mass component of the Taurus population and can be placed in the context of the full spectrum of disks by combining with previous results on higher-mass Taurus members. The results from an SMA snapshot survey combined with previous single-dish measurements provide a catalog of measured or extrapolated 890 μm flux densities for a sample of 179 Taurus systems (Andrews et al. 2013), to which the 24

ALMA results are added. The stellar mass of each Taurus member observed in either study is determined by relating the spectral type of the target to a corresponding effective temperature scaling from Herczeg & Hillenbrand (2014), a comparison of the evolutionary models of Baraffe et al. (1998) and Baraffe et al. (2015, hereafter BHAC15), and the Modules for Experiments in Stellar Astrophysics (MESA) Isochrones and Stellar Tracks (MIST) models for higher-mass targets (Choi et al. 2016). Estimation of central object mass via spectral type has been performed in previous studies (e.g., Kraus & Hillenbrand 2007; Pascucci et al. 2016), either alone or in tandem with other mass estimation approaches (e.g., model comparison with SED estimates of temperature and luminosity). In this study, we adopt a uniform mass estimation approach for all objects based on spectral type to avoid ambiguities in luminosity/age estimation due to the presence of edge-on disks. Further description of the mass and luminosity estimation method for the central stars/brown dwarfs is provided in greater detail in Appendix A.

The masses adopted from the new BHAC15 and MIST models are updated from those reported in the Andrews et al. (2013) compilation, which utilized an older suite of models (D'Antona & Mazzitelli 1997; Baraffe et al. 1998; Siess
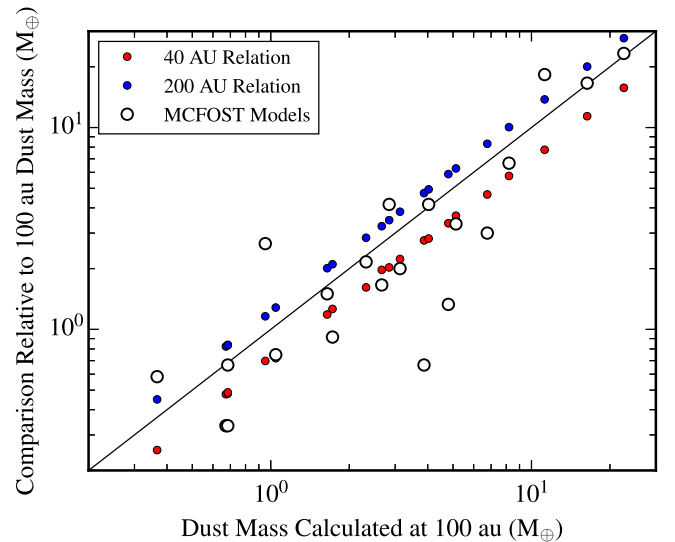
Table 10
Genetic Algorithm Results with SED Fitting in MCFOST

| Target	$M_{\rm dust}$ ($M_\oplus$)	H_0 (au)	$r_{\rm in}$ (au)	β	Surf. Dens.	χ^2
J04144730	3.00	18.5	0.01	1.2	−0.65	45
J04161210	2.16	23.5	0.05	1.2	−1.4	100
J04181710	0.33	23.5	0.02	1.08	−0.5	10
J04190110	0.10	18	1	1	−1.05	500
J04202555	6.66	14.5	0.4	1.2	−0.35	55
J04213459	0.11	17.5	0.04	1.25	−1.25	125
J04230607	2.00	16	0.08	1.2	−0.75	15
J04262939	4.16	18.5	0.04	1.08	−0.3	13
J04284263	0.67	18	0.02	1.08	−0.75	58
J04292165	0.67	22.5	0.05	1.08	−0.4	42
J04322210	23.31	11	0.05	1.27	−0.8	35
J04334465	16.65	14	0.05	1.08	−0.9	16
J04381486	2.66	25	0.03	1	−1.4	600
J04382134	1.50	20	0.02	1	−1.2	20
J04385859	18.31	10.5	0.08	1.09	−0.4	9
J04390163	0.33	12	0.02	1.07	−0.55	10
J04390396	0.92	19.5	0.04	1.1	−0.25	33
J04393364	4.16	15	0.08	1.06	−0.55	17
J04394488	1.33	20	0.08	1.16	−0.5	45
J04400067	3.33	10.5	0.11	1.23	−0.8	60
J04414825	1.66	20	0.9	1.13	−1	35
J04555605	0.58	18	0.3	1.3	−1.4	500
J05075496	0.75	16.5	0.07	1.14	−0.4	10

Figure 9. Comparison of the MCFOST model disk dust masses and the analytically derived masses, calculated as described in Section 6.1. Estimated analytic masses assuming disk radii of 40 and 200 au (red and blue circles, respectively) and masses derived from MCFOST radiative transfer modeling (open circles) are compared against the analytic result for a 100 au disk case on the *x*-axis. The black line represents the one-to-one relationship for the 100 au case plotted against itself. The MCFOST model results agree well within the ranges of masses inferred from the 40–200 au analytic estimates and appear more consistent with the 40 au disk dust masses.

et al. 2000) that yield systematically lower masses at lower luminosities and higher masses at higher luminosities. The disk masses of the sources detected with the SMA or single-dish surveys are estimated with Equations (1) and (3) and plotted in Figure 10 as a function of object mass utilizing the dust temperature–luminosity scaling described in Section 6.1. In Figure 10, the uncertainties in dust mass are derived from dust temperatures incorporating a range of disk sizes centered at 100 au disks, with the lower estimate of dust mass corresponding to 40 au disks and upper estimate corresponding to 200 au disks, and include the impact of a 10% systematic uncertainty in flux.

Like the more massive host stars, the low-mass ALMA-detected sources exhibit a large spread in disk mass for a given host mass, since the sensitivity limit is sufficient to detect most disks and not only the upper envelope of sources. To gauge the decline in disk mass as a function of central object mass, two comparison lines assuming a gas-to-dust ratio of 100:1 are also plotted, representing disks of 0.2% and 0.6% of the mass of the central object. The 0.2%–0.6% range, corresponding to the average scaling factor for the linear $M_{\rm disk} \sim M_{\rm star}$ range found by Andrews et al. (2013), intercepts the median high-mass Taurus targets and the least-massive disks for the lowest-mass hosts. With the large dispersion in dust mass at any given stellar mass, significant populations exist above and below the relations.

Best-fit power laws to the detections and upper limits for the Taurus population are shown in Figure 11 (red points and lines), applying the Bayesian linear regression approach of Kelly (2007) to incorporate both detections and upper limits. With greater numbers of targets at lower host masses, the Taurus best-fit relation of $\log[M_{\rm dust}(M_\oplus)] = (0.97 \pm 0.14)$ $\log[M_{\rm star}(M_\odot)] + (1.15 \pm 0.09)$ with an intrinsic scatter of 0.49 dex in $\log[M_{\rm dust}(M_\oplus)]$ is consistent with a linear relation,

similar to the relations reported for disks around Taurus stellar hosts in Andrews et al. (2013), and the TBOSS data are consistent with the general trend of decreasing disk mass with declining central object mass, suggesting a common formation mechanism across the full mass spectrum.

6.4. Disk Mass as a Function of Time and Environment

To investigate the evolution of the disk dust mass, dust mass as a function of host mass is also plotted for the region of Upper Sco in Figure 11 (blue points and lines). The Taurus component is the same as in Figure 10, described in Section 6.1. To explore the full range of stellar masses for targets in Upper Sco, a compilation of studies is used for comparison, with values drawn from a single-dish IRAM survey of high-mass Upper Sco members (Mathews et al. 2012) and a large recent ALMA study (Barenfeld et al. 2016). For the lowest-mass hosts, the results from the Taurus ALMA sample are compared with our ALMA pilot study of brown-dwarf Upper Sco members (van der Plas et al. 2016). Both samples of brown dwarfs are too small in number and too biased toward detections to address the frequency of submillimeter-detected disks over time, but the measured flux densities converted to disk masses can be used to study how the mass changes with age. Dust masses for all targets in Upper Sco were reestimated with a self-consistent approach using Equations (2) and (3) (see Appendix B). While a considerable range of disk masses is present for any given object mass, and the lowest-mass systems in Taurus overlap with the highest-mass examples in Upper Sco, there is a clear drop in the overall disk-mass level with time. The ages of the two samples, with ∼1–2 Myr for Taurus (e.g., Kraus & Hillenbrand 2009) and ∼5–10 Myr for Upper Sco (Blaauw 1978; Pecaut et al. 2012), cover important timescales in planet formation and disk evolution, including formation of giant planets by gravitational instability (<1 Myr;
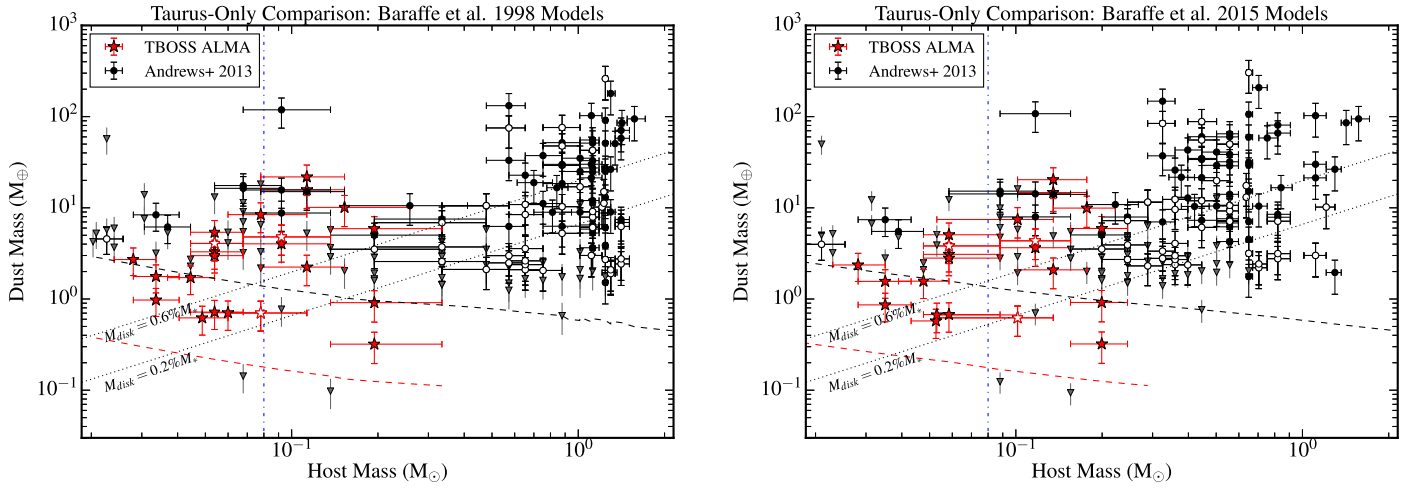
Figure 10. Taurus-only disk dust mass vs. object mass for detections within our sample (red stars) and the full Class II Taurus population with submillimeter detections from Andrews et al. (2013; black symbols). Stellar parameters are derived from spectral types and the evolutionary models of Baraffe et al. (1998; left) and BHAC15 (right), assuming an age of 1 Myr. The x-axis error bars correspond to the possible range of derived stellar masses assuming ±0.5 subclass error on the spectral type. The y-axis error bars correspond to the range of dust mass within the disks, assuming at minimum a disk radius of 40 au (lower limit) and maximum of 200 au (upper limit), and incorporate a 10% absolute flux calibration uncertainty. Open symbols correspond to identified binaries. Upper limits are provided as downward-pointing triangles, with the range denoting disk masses evaluated at disk radii of 40, 100, and 200 au. Overlaid in dashed lines are the 3σ sensitivity limits for our survey (0.39 mJy; red line) and Andrews et al. (2013; 3 mJy; black line). Also shown are the lines of disk mass proportional to stellar mass (dotted black lines) and the stellar/substellar boundary at 0.08 $M_\odot$ (blue dash-dotted line).
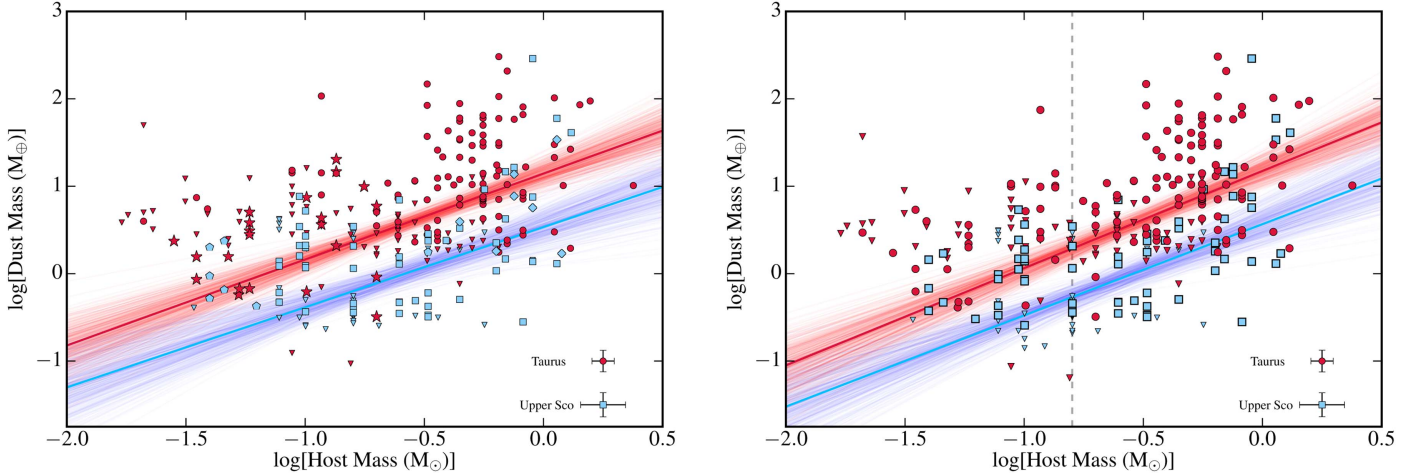
Figure 11. Disk dust mass as a function of stellar host mass for Taurus and Upper Sco with overlaid power-law fits to combined detections and upper limits. (Left) With a single disk size of 100 au for all objects and uncertainties (in the corner) incorporating disk sizes ranging from 40 to 200 au, the best-fit linear regression for Taurus is $\log[M_{\rm dust}(M_\oplus)] = (0.97 \pm 0.14)\log[M_{\rm star}(M_\odot)] + (1.15 \pm 0.09)$ with 0.49 dex of intrinsic scatter (red lines), and for Upper Sco it is $\log[M_{\rm dust}(M_\oplus)] = (0.92 \pm 0.18)\log[M_{\rm star}(M_\odot)] + (0.46 \pm 0.09)$ with 0.54 dex of intrinsic scatter (blue lines). Symbols for combined studies include this work (stars) and Andrews et al. (2013; circles) for Taurus in red and van der Plas et al. (2016; pentagons), Barenfeld et al. (2016; squares), and Mathews et al. (2012; diamonds) in blue for Upper Sco. The slopes between the Taurus and Upper Sco populations are similar within uncertainties. Dust mass and stellar mass estimations assume a population age of 10 Myr for Upper Sco vs. 1 Myr for Taurus. The three previous Upper Sco surveys cover a wide range of stellar masses and have significantly lower dust masses, corresponding to an approximately 0.5 dex decrease between the two populations. (Right) Assuming disk sizes of 40 au for targets M4 and later and 100 au disks for <M4 (demarcated by the vertical dashed line), the slopes are slightly steeper (1.11 ± 0.14 for Taurus; 1.05 ± 0.18 for Upper Sco) but agree with the 100 au case within uncertainties. The uncertainties (in the corner) include a range of disk sizes from 20 to 100 au.

Boss 1997) or core accretion (~10 Myr; e.g., Pollack et al. 1996), the onset of terrestrial planet formation (~3–10 Myr; Chambers & Wetherill 1998), and the dissipation of gas-rich primordial disks (~3 Myr; Luhman et al. 2010).

Applying the same linear regression analysis to the Upper Sco populations, the best-fit Upper Sco power-law relation of $\log[M_{\rm dust}(M_\oplus)] = (0.92 \pm 0.18) \log[M_{\rm star}(M_\odot)] + (0.46\pm0.09)$ with an intrinsic scatter of 0.54 dex in $\log[M_{\rm dust}(M_\oplus)]$ has a slope similar to that of the Taurus population fit in Section 6.3 within uncertainties, and the

combined populations are shown in Figure 11. The comparison between intercepts of the fits to each of the two regions suggests a decline in disk mass by a factor of ~4–5 over the critical ~1–10 Myr time period between Taurus and Upper Sco, similar to the conclusion reached in previous studies (Ansdell et al. 2016). The total gas and dust disk-mass decline is probably significantly larger than indicated by the drop in fit intercept values, as the gas-to-dust ratio likely evolves over time, since Upper Sco targets typically only have upper limits (van der Plas et al. 2016).

Table 11
Calculated Slopes for Taurus and Upper Sco Compilations

Disk Size	Taurus G8–M8.5	U. Sco G7–M7.5
Uniform 100 au	0.98 ± 0.14	0.92 ± 0.18
Uniform 100 au (det. only)	0.65 ± 0.11	0.42 ± 0.16
40 au (M4+), 100 au (<M4)	1.11 ± 0.14	1.05 ± 0.18
20 au (M4+), 100 au (<M4)	1.23 ± 0.14	1.16 ± 0.18

To measure the impact of adopting 100 au disk sizes for all of the objects, the Taurus and Upper Sco samples were broken into separate subsets at the M4 spectral type. Smaller disk radii of either 20 or 40 au were then assumed for the M4 and later spectral types, with uncertainties corresponding to disk sizes from 10 to 100 au in the 20 au case or 20 to 100 au in the 40 au case. Figure 11 shows the fit to the populations with the 40 au disk size for lower-mass objects. The slopes from the tests are listed in Table 11, showing that the results are within the uncertainty of the fit with the assumption of 100 au disks for all object masses. Regardless of the assumed disk size for the low-mass component of the population, the Taurus and Upper Sco slopes are within 1σ of each other. Finally, two separate power-law fits were made to the Taurus population, splitting the sample at either the M4 or M6 spectral type. The slopes for the high- and low-mass members are consistent within 2σ of each other for a dividing spectral type of M4. The sample of substellar objects with spectral type M6 or later was too small to conduct a meaningful similar test; the fit to the brown-dwarf population was unconstrained, ranging from positive to negative slopes. Within the limitations imposed by the current sample sizes, the brown-dwarf disks do not appear to either dissipate more quickly than their counterpart disks above the substellar limit or retain an elevated amount of disk dust material over time.

The fitted slope of 0.92 ± 0.18 for the combined Upper Sco population reported here is shallower than that of 1.67 ± 0.37 reported in the large recent ALMA Upper Sco survey by Barenfeld et al. (2016), and we investigate the source of the discrepancy. The additional detections and limits from van der Plas et al. (2016) and Mathews et al. (2012) do not change the slope at a significant level relative to including only the sample of Barenfeld et al. (2016). Full details of the $M_{\rm dust}$ and $M_{\rm object}$ comparisons for Upper Sco are given in Appendix B, and the results show that the key factor is the slope sensitivity to the choice of stellar evolutionary models: Siess et al. (2000) models in the Barenfeld et al. (2016) analysis and the more recent Baraffe et al. (2015) models in this study. (Repeating our fitting technique for the Barenfeld et al. population with our recalculated dust masses and their published stellar masses results in a slope of 1.87 ± 0.34, consistent with the Barenfeld et al. 2016 result.) Considering various treatments of dust temperature and stellar mass/luminosity, the range of slopes for both Taurus and Upper Sco reported within previous Taurus/Upper Sco surveys and recent ALMA surveys of regions such as Lupus III and Chamaeleon (e.g., Ansdell et al. 2016; Pascucci et al. 2016) have been consistent with both linear and steeper-than-linear relations. The choice of stellar evolutionary models and dust temperature relations are thus important factors in determining slope steepness, and the fit parameters can only be compared if a uniform approach is adopted for all regions.

To enable a comparison with a low-mass population at approximately the same age as Taurus but in a different star-
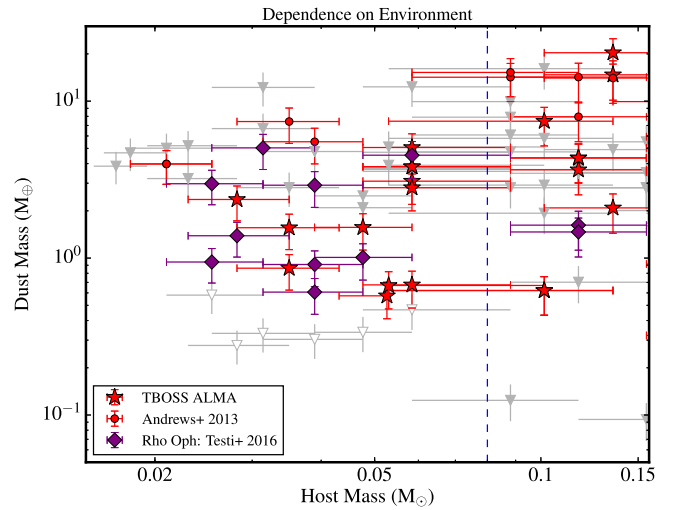

Figure 12. Comparison of the Taurus lowest-mass stars and brown dwarfs from Andrews et al. (2013) and our survey (red points and stars) and the ρ Ophiuchus population reported in Testi et al. (2016; purple diamonds). Upper limits are shown as open triangles for ρ Oph and filled triangles for Taurus. While the ages of the star-forming regions are thought to be similar at $\sim$1 Myr, no statistically significant difference in dust mass is observed between the two regions, suggesting that any differing environmental effects may not be significant. The boundary between the stellar and substellar limit (0.08 $M_{\odot}$) is shown with the vertical dashed line.

forming environment, the brown-dwarf population of ρ Ophiuchus investigated by Testi et al. (2016), also with ALMA, is shown for comparison with the Taurus population in Figure 12. The Taurus and ρ Ophiuchus populations show similar mean and variance in dust masses for disk hosts with central object masses $<0.08 \, M_{\odot}$ (Taurus = $2.1 \pm 1.4 \, M_{\oplus}$, ρ Oph = $2.3 \pm 1.6 \, M_{\oplus}$). A two-sample Anderson–Darling (AD) test produced no statistically significant difference in dust mass within brown-dwarf and low-mass star disks between TBOSS and ρ Oph (AD-statistic = 0.02, critical value for 5% significance of 1.961, approximate p-value = 0.34).
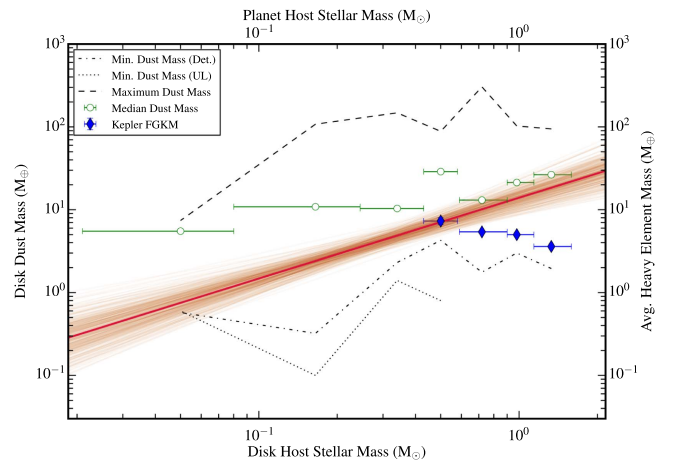
6.5. Implications for Planet Formation

The observed exoplanet population can provide insight into the amount of planet-forming material that must be available within primordial disks, enabling a comparison with the mass inventory in dust estimated from submillimeter flux densities of young Taurus objects. The average heavy-element mass required to form the population of *Kepler*-detected 2–50 day period planets was inferred by Mulders et al. (2015). The *Kepler*-inferred heavy-element masses are plotted in Figure 13, along with the Taurus ALMA results. Since the *Kepler* results are confined to short-period planets corresponding to a limited radius within the disks, we also make a comparison with the minimum-mass solar nebula (MMSN; $\sim$35 $M_{\oplus}$ dust, $\sim$11 $M_{\rm Jup}$ gas+dust; Weidenschilling 1977), since this covers the entire extent of the planetary system. This is, however, a solar system–centric comparison, and it is not currently known how representative the MMSN is of a typical planetary system. Indeed, we know that many exoplanetary systems look very different from the solar system. In particular, it might well be expected that even if the MMSN is reasonably representative of G-type stars, it may not be applicable to other spectral types (cf. a minimum-mass M-dwarf nebula of 53 $M_{\oplus}$ of condensates for hosts of stellar mass 0.46 $M_{\odot}$; Gaidos 2017).
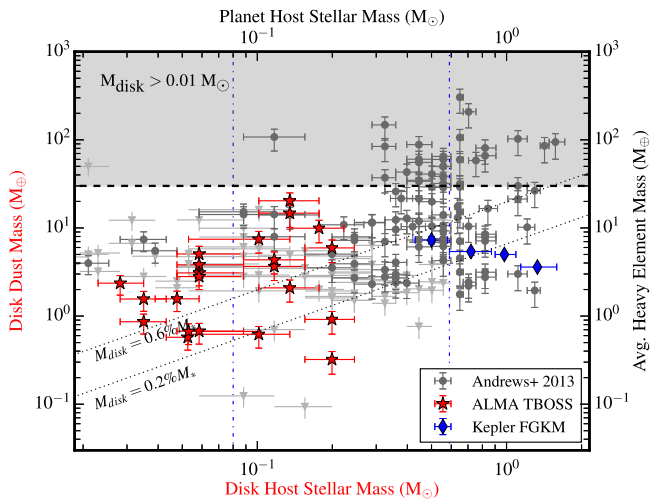
Figure 13. Comparison of our derived dust masses and the dust masses for higher-mass Taurus members from Andrews et al. (2013) with the heavy-element distribution inferred from *Kepler* FGKM stars (Mulders et al. 2015; blue diamonds) and the giant planet–forming limit for the total mass of the disk (gas+dust) from the MMSN, assuming a gas-to-dust ratio of 100:1 (gray shaded region). Upper limits for the combined Taurus disk samples are shown as downward-pointing triangles, and blue dot-dashed lines denote the range of main-sequence M dwarfs down to the 0.08 $M_\odot$ limit.

Figure 14. Comparison of the median, minimum (detections and upper limits), and maximum dust masses for Taurus in terms of disk dust mass ($M_\oplus$) as a function of the host stellar mass ($M_\odot$). As in Figure 13, the *Kepler* FGKM heavy-element masses estimated from Mulders et al. (2015) are shown as blue diamonds (with the right *y*-axis and upper *x*-axis corresponding to the heavy-element masses and *Kepler* host star masses, respectively). The corresponding binned dust mass values are provided in Table 13, and the overplotted linear regressions correspond to the Taurus best fit with 100 au disks in Figure 11.

The *Kepler* planet host masses are determined from the stellar effective temperature and mass table given in Pecaut & Mamajek (2013) and the *Kepler* host star planets compiled in Mulders et al. (2015). Over 90% of the M-star hosts analyzed by Mulders et al. (2015) are M0–M3, and so the host mass range of the *Kepler* results only extends down to ∼0.4 $M_\odot$, as plotted in Figures 13 and 14. The *Kepler* and Taurus disk population results are summarized for comparison over common mass ranges in Table 12, which also quantifies the proportion of Class II disks that exceed the average heavy-element mass estimated from *Kepler* and the MMSN. Table 13 reports the minimum (both for detections and limits), maximum, and median (including limits) disk dust mass values for the same mass ranges. The heavy-element masses from Mulders et al. (2015) trend upward toward lower stellar masses for planetary systems with 2–50 day orbital periods. As shown in the dispersion of the points in Figure 13 and the upper and lower envelopes in Figure 14, the majority (57%) of the Taurus sample has larger masses present in small particles than ultimately coalesce into planets with short periods measurable with *Kepler*, and a smaller but still significant fraction (24%) contains more mass in dust than the MMSN. Considering only the best-fit relation for the full Taurus Class II population plotted in Figure 14, the fit to disk dust mass exceeds the mass inventory in exoplanets around higher-mass stars and intercepts the expected exoplanet inventory for the lowest-mass hosts considered in the *Kepler* study. From an ALMA survey of Cha I Class II members, Pascucci et al. (2016) similarly found that the best fit to the disk dust masses in Cha I is greater than the estimated material locked within the close-in exoplanet population for $\gtrsim 1\,M_\odot$ stars, but that the least-massive (0.4 $M_\odot$) Cha I hosts have median disk masses a factor of 2 lower than the average mass in exoplanets. Although the median Cha I value for M-star hosts is lower than the inferred *Kepler* value, the large dispersion in dust mass observed in Cha I (similar to Taurus) is such that part of the M-star

population retains disks with dust masses comparable to or larger than the *Kepler* average heavy-element mass.

While our observations explore a range of grain sizes on the order of the observation wavelength, an outstanding question remains as to the fraction of mass in undetectable larger bodies by the age of Taurus. By the age of 1–2 Myr, the rate of dust detection in infrared and submillimeter/cm surveys suggests that coagulation mechanisms in simulations, while efficient at growing grains up from submicron scales, are insufficient to maintain the small-grain dust population on their own, which must be replenished. This could be achieved with an equilibrium reached between growth and collisional grinding and fragmentation processes (Dullemond & Dominik 2005). The model from Dullemond & Dominik (2005) incorporating coagulation with the effects of grain settling and mixing, as well as fragmentation, suggests that near ∼1 Myr, an approximately 0.5 dex greater mass surface density of the disk is contained within cm-sized grains than submillimeter grains within a simulated vertical slice at 1 au. This factor of ∼3 in mass surface density can be compared with the observational results from longer-wavelength studies of disks from the same or similar star-forming regions. For an M1 member of Taurus-Auriga, CY Tau, Pérez et al. (2015) analyzed spatially resolved continuum measurements at 1.3, 2.8, and 7.1 mm from the Disks@EVLA program. They found best-fit model parameters on the disk structure which, at a radius of 1 au, correspond well with the surface density ratio of ∼3× more mass in larger grains inferred from Dullemond & Dominik (2005) for the ratio of mass surface density from 1.3 to 7.1 mm. However, with resolved measurements, Pérez et al. found that the grain size distribution is strongly dependent on location within the disk, corresponding to a much larger population of small grains in the outer disk and providing strong evidence for radial drift effects. As the Dullemond & Dominik (2005) models present a simple case excluding factors such as radial drift and runaway growth, it is likely that simply scaling the sub-millimeter-inferred dust mass by a factor of 3× presents a limiting case for mass in submillimeter-to-cm-sized objects.

Table 12
Disk Detection and Dust Mass Frequencies Relative to Class II and III Populations, with Corresponding Heavy-element Masses from the
Short-period *Kepler* Planet Statistics and the Fraction of Disks Reaching MMSN Values

Main-sequence Spectral Type	F Stars	G Stars	K Stars	Early-M	Mid-M	Late-M	Substellar
Mass range ($M_\odot$)	1.14–1.59	0.9–1.14	0.59–0.9	0.43–0.59	0.245–0.43	0.08–0.245	⩽0.08
Num. Class II observed	5	4	26	38	48	45	33
% Class II > avg. heavy elem. mass	80	75	69	57	…	…	…
% Class II > MMSN	20	40	19	24	7	1	0
Num. Class III	5	1	17	12	13	37	42
% submm det. in Class II+III	50	80	58	58	41	24	19

Table 13
Disk Dust Mass Values for Various Host Mass Regimes in Taurus,
Combining This Study and Andrews et al. (2013)

Object	Taurus Class II ($M_\oplus$)				*Kepler*
M_* ($M_\odot$)	Min. (UL)	Min. (Det.)	Max.	Med.	Avg.
1.14–1.59	…	2.0	94.5	26.5	3.6
0.9–1.14	…	3.0	102.6	21.3	5.0
0.59–0.9	…	1.8	303.8	13.1	5.4
0.43–0.59	0.8	4.3	88.3	28.9	7.3
0.245–0.43	1.4	2.3	147.8	10.4	…
0.08–0.245	0.1	0.3	107.7	10.9	…
⩽0.08	0.6	0.6	7.4	5.1	…

Note. Disk minimum values from upper limits denoted by UL, and *Kepler*
estimates from Mulders et al. (2015).

Figure 15. Cumulative distributions showing estimated total (gas+dust) disk masses as a fraction of total disk mass to stellar mass, assuming a gas-to-dust ratio of 100:1. The blue dashed line indicates the gravitationally unstable limit ($M_{disk} = 0.1\,M_{star}$), and the black dashed line indicates the median. Taurus populations are from this study and Andrews et al. (2013; red curve), using analytically derived masses assuming $r = 100$ au disks. Upper limits are incorporated using Kaplan–Meier estimation, with distribution width indicating 1σ confidence intervals. The Upper Sco population (green curve) is a combined distribution from Mathews et al. (2012), Barenfeld et al. (2016), and van der Plas et al. (2016), also incorporating upper limits. The yellow hatched distribution indicates a limiting case of extrapolating the Taurus mass in cm-sized grains as $3\times$ the measured submillimeter dust masses, in which case ~35% of Taurus systems would be gravitationally unstable.

To illustrate the distributions of disk masses derived from submillimeter observations and the potential impact of scaling up the Taurus disk masses to also include ~cm-sized grains, we show the cumulative distributions of systems as a fraction of the gravitationally unstable disk-mass limit in Figure 15. The gas-to-dust ratio is assumed to be 100:1, as for the interstellar medium (ISM), and the limit for a gravitationally unstable disk is taken as $M_{disk} = 0.1\,M_{star}$. This places a representative upper limit on the possible mass of the disk and constrains the range of possible "unseen" mass in larger bodies within the disk. Note that while it is possible that the gas-to-dust ratio at the age of Taurus is lower than 100:1, it would presumably have started at the ISM value, and thus the gravitational stability limit we are comparing to would still have applied earlier in the disk evolution. As seen in Figure 15, it is notable that the shape of the older Upper Sco distribution is very similar to that of the Taurus population, suggesting that the decrease in dust mass between the ages of Taurus and Upper Sco occurs uniformly across the distributions. For comparison, a scenario with $3\times$ the submillimeter dust mass in cm-sized grains is also shown for the Taurus samples (yellow hatched distribution). This leads to around 30%–40% of systems exceeding the gravitationally unstable mass, suggesting that the mass in larger objects not seen by our ALMA observations is not this large and that in many cases the dust we observe in the submillimeter constitutes the bulk of the mass of solid particles in the disk. As such, at the age of Taurus, planet formation may be in its very early stages.

To place these timescales within the context of our own solar system, isotopic studies have also placed limits upon the formation timescales of small grains and early parent bodies (Chambers 2010), including calcium aluminum-rich inclusions (CAIs; ⩽0.2 Myr), iron meteorites (⩽1 Myr), chondrules

(1–3.5 Myr), and the cores of Mars and Vesta (ranging from 1 to 10 Myr, although earlier ages of 1.8 Myr for Mars have been posited; Dauphas & Pourmand 2011). Given the relative size scales of CAIs and chondrules in meteorites, on the order of submillimeter and cm-sized grains, these timescales correspond well to the significant abundance of similar-sized grains detected in submillimeter/mm surveys of protoplanetary disks. Furthermore, the depletion when comparing with Upper Sco suggests that the majority of planet formation may be taking place between these age ranges, which would also be in agreement with the formation timescales of larger planetesimals in the solar system.

Theoretical models of giant planet formation (e.g., Alibert et al. 2005) suggest that the MMSN is also roughly the minimum mass required for the formation of giant planets. As shown in Figure 13, while the upper envelope of disk masses exceeds this for hosts with masses above the stellar limit, this is not true for hosts below the stellar/substellar boundary. This suggests that the disks of substellar objects are not massive enough to support giant planet formation within the disks, and that planetary-mass companions identified around

brown-dwarf primaries such as 2M1207b and 2M J044144 (Chauvin et al. 2004; Todorov et al. 2010) may form through a process similar to that of binary stars rather than within a planet-forming disk. This suggestion is reinforced by examining the 193 Taurus Class II and Class III objects with masses in the 0.08–0.6 $M_\odot$ range (equivalent to main-sequence M dwarfs). Of these 193 objects summarized in Table 12, 32 (17%) have disk masses larger than the MMSN and thus are theoretically amenable to giant planet formation; this frequency assumes that no Class III members have MMSN disks, although there is no comparably deep submillimeter survey of Class III members. By comparison, large-scale exoplanet surveys indicate that the occurrence rate of giant planets around M dwarfs is ∼2% out to orbits probed by radial-velocity surveys (∼5.5 yr; e.g., Cumming et al. 2008; Johnson et al. 2011), and deep AO imaging surveys for giant planet companions to M stars have reported null detections over the ∼10–100 au range (e.g., Bowler 2016). Comparison of the frequencies of MMSN disks and M-star giant planets suggests that the efficiency of forming giant planets from MMSN disks is close to ∼10%, and most disks that are theoretically capable of forming giant planets, at least around low-mass hosts, do not do so.

7. Summary and Conclusions

In summary, the detections from this initial ALMA Cycle 1 study of 24 M4–M7.75 Class II Taurus members (21 detections at >8σ, one marginal detection at 5σ, and two nondetections) show that the dramatic increase in sensitivity achieved with ALMA combined with a target selection based on *Herschel* PACS 70 μm fluxes (Bulger et al. 2014) enables investigations of the disk properties of the full host mass spectrum of young star-forming regions. The targets represent half of the Class II members in this spectral-type range with *Herschel* detections and span the full range of PACS 70 μm fluxes rather than a subset of the brightest members. This pilot study includes seven transition disks and one truncated disk, and the nondetections are both transition disks, though other objects in this class are among the brightest ALMA detections; the truncated disk is the most marginal detection.

The 885 μm continuum flux densities that are the subject of this paper range from 1.0 to 55.7 mJy. The results from the spectral line observations covering the ^{12}CO(3–2) emission will be reported in the next paper in the TBOSS series (G. van der Plas et al. 2018, in preparation). Applying different approaches to converting the flux densities to dust masses—several scaling laws and radiative transfer modeling with MCFOST—results in a factor of 2.5 range in mass estimates, with the radiative transfer model estimate typically at the lower part of the mass range inferred from scaling laws based on different disk radii (Andrews et al. 2013; van der Plas et al. 2016). By employing the relations in Equations (1) and (3) that can be applied to all Taurus members with submillimeter detections, the dust masses for the TBOSS ALMA sample range from 0.3 to 20 $M_\oplus$, comparable to several times the mass of Mars to enough Earth masses to form a giant planet core (Pollack et al. 1996).

Combining the new ALMA results with the disks around more massive Taurus members shows a trend of declining disk dust mass with central object mass with a large amount of scatter (at least one order of magnitude) at any given mass. Considering a range of outer disk radii for the low-mass object disks, the slope of the power-law fit to the $M_{\rm dust}$ versus $M_{\rm object}$ relation is consistent with linear over the host mass range of

∼35 $M_{\rm Jup}$–1 $M_\odot$, which encompasses most of Taurus. The specific value of the slope is very dependent on the choice of evolutionary model to determine the object masses, and a steeper-than-linear slope is obtained with a different model set. The brown-dwarf disk population appears as a continuous extension of the low-mass stars rather than a distinct set.

Comparing the Taurus-detected disks with results from low-mass stars and brown dwarfs in the older Upper Sco region shows that the Upper Sco members have disk masses comparable to or lower than the lowest-mass disks around similar-mass host objects. In contrast to the larger dust masses in Taurus, the decline in mass of the dust in small (≲1 mm) particles in Upper Sco may be an indication that planet formation has progressed to the stage in which most solids are in the form of planetesimals and planets and undetectable at submillimeter wavelengths. It has long been noted that giant planet formation must be complete before the gas disk dissipates so that they can accrete their gaseous envelopes. Modern theories for the growth of solid planetesimals, such as the streaming instability (e.g., Youdin & Goodman 2005; Johansen & Youdin 2007; Youdin & Johansen 2007) and pebble accretion (e.g., Lambrechts & Johansen 2012; Levison et al. 2015a, 2015b), which apply to both terrestrial planets and giant planet cores, proceed rapidly once the processes are initiated and also rely on the presence of gas. Furthermore, isotopic analysis of solar system meteorites indicates that large bodies had formed within a few million years of the condensation of the first solids (e.g., Connelly et al. 2008, 2012; Bouvier & Wadhwa 2010). As such, the decline in dust mass from Taurus to Upper Sco is aligned with theoretical expectations for planet formation.

The mass inventory of solids in small particles detected by submillimeter emission typically exceeds the average heavy-element mass inferred from *Kepler* short-period planetary systems (Mulders et al. 2015). This comparison quantifies that a sufficient mass reservoir exists to form the super-Earth and mini-Neptune planets that constitute the bulk of the *Kepler* exoplanet discoveries and that the timescale for formation may exceed the ∼1–2 Myr age of Taurus. While the majority of disks appear to be sites conducive to small planet formation, a much lower proportion of disks have a total mass large enough for giant planet formation based on a standard 100:1 gas-to-dust ratio and a threshold disk mass of ∼0.01 $M_\odot$ (Alibert et al. 2005). Under these assumptions, few low-mass stars have disk masses meeting or exceeding the MMSN limit, commensurate with the limited numbers of giant planets detected around these hosts to date. Direct-imaging searches for sub-Jovian M-dwarf exoplanets with upcoming facilities like the *James Webb Space Telescope (JWST)* anticipate reaching expected mass limits of ∼2 times that of Neptune (Schlieder et al. 2016), and the disk dust mass results suggest that higher-mass M dwarfs may be more amenable to hosting low-mass gas/ice giant exoplanets than the lowest-mass M-dwarf hosts. Applying solar system proportions of dust and ice in solids (rocky material ∼1/3 and ice ∼2/3; Lodders 2003) to the composition of Neptune (∼13–15 $M_\oplus$ in heavy elements; Helled et al. 2011) suggests that ∼4–5 $M_\oplus$ in dust is required to form a Neptune-like planet. In a rough analogy to the MMSN estimate of the disk required to form a Jupiter-like planet, the minimum-mass dust disk required to form a Neptune would contain ∼5 $M_\oplus$ in rocky material, or ∼10 $M_\oplus$ for the expected 2× Neptune *JWST* imaging detection limit. As

seen in Figure 13, few late-M Taurus disks contain $\sim 10\, M_\oplus$ in dust particles measurable with ALMA.

Among Taurus members with masses in the range of main-sequence M stars (0.08–0.6 $M_\odot$), the frequency of observed candidate giant planet–forming disks is 17%. This value exceeds the $\sim 2\%$–3% frequency of M-dwarf giant planets for periods $<10^4$ days derived from the synthesis of radial-velocity and microlensing surveys (e.g., Clanton & Gaudi 2014) and, with the null detection of wider-orbit planets in M-dwarf direct-imaging surveys (e.g., Bowler et al. 2015), suggests a relatively low efficiency for giant planet formation. By contrast, none of the brown-dwarf Taurus members have total disk-mass estimates above the giant planet formation threshold, suggesting that imaged planetary-mass companions to brown dwarfs did not originate in disks.

Appendix A
Central Object Spectral Type, Temperatures, and Masses

A uniform procedure was applied to estimate the central object mass for all of the Taurus, Upper Sco, and ρ Oph members considered in this study of disk mass as a function of host mass (Figures 10–14).[16] The observable measured for all objects is the spectral type, and the transformation to mass required two main steps: (1) converting spectral type to effective temperature ($T_{\rm eff}$) with an empirical relation and (2) converting $T_{\rm eff}$ into mass with theoretical evolutionary models. The impact due to the choice of age and evolutionary model was investigated, and comparisons with previous results for Taurus members were explored. Overall, the adopted evolutionary model had the largest effect on mass estimation, more important than the specific age assumed for the region or the spectral type–$T_{\rm eff}$ relation.

The empirical relation developed to convert observed spectral types into effective temperatures is shown in Figure 16 (Herczeg & Hillenbrand 2014). This more recent transformation builds upon the relationship developed in Luhman et al. (2003) and covers a larger range of spectral types, and we applied a least-squared univariate spline interpolation to this relation to account for noninteger spectral types. Table 14 reports the spectral types and uncertainties from the literature along with the estimated $T_{\rm eff}$ for all objects considered in this study from Taurus (Andrews et al. 2013), Upper Sco (Mathews et al. 2012; Barenfeld et al. 2016; van der Plas et al. 2016), and ρ Oph (Testi et al. 2016). The most recent spectral type is used for sources with multiple values, and an uncertainty of ± 0.5 subclasses is applied to any object without a reported uncertainty.

Combining the effective temperature with an age, the mass was estimated in conjunction with an evolutionary model. Typical ages reported for the Taurus region range from 0 to 5 Myr, with isochrone fitting to the cluster sequence tracing a canonical value of 1–2 Myr (Kraus & Hillenbrand 2009). For objects cooler than ~ 4500 K, the evolutionary models of Baraffe et al. (1998) have been widely adopted, although the updated grid from Baraffe et al. (2015) is now available. Figures 17 and 18 show the impact of the choice of age and evolutionary model for the cooler Taurus members and highlight that the evolutionary model has the dominant systematic effect on the mass estimation, with the newer models yielding a lower mass for the same effective temperature. For this study, an age of 1 Myr and the Baraffe et al. (2015) model grid were used in the mass determination for objects with $T_{\rm eff} \leqslant 4211$ K, corresponding to spectral types of approximately K7 or later. For earlier spectral types with higher effective temperatures, the MIST models (Choi et al. 2016) were applied, and the full mass versus $T_{\rm eff}$ sequences for 1 and 2 Myr models are shown in Figures 19 and 20. The newer Baraffe et al. (2015) models connect with the MIST models. Figures 19 and 20 also plot the luminosity as a function of $T_{\rm eff}$ from the evolutionary models, since the central object luminosity is required to estimate the disk

---

[16] Example analysis scripts and auxiliary data for the methods described in Appendices A and B are available at https://osf.io/9dyx4.

Table 14
Rederived Stellar Parameters and Dust Masses for Our Sample and Comparison Samples

Name	Source	Region	Age (Myr)	SpTy	T_{eff} (K)	Stellar Mass ($M_\odot$)	Log L_* ($L_\odot$)	M_{dust40} ($M_\oplus$)	$M_{dust100}$ ($M_\oplus$)	$M_{dust200}$ ($M_\oplus$)
J04292165	(1)	Taurus	1	M6	2858	0.06 {0.05, 0.09}	−1.57 {−1.69, −1.24}	2.72	3.82	4.67
J04141188	(1)	Taurus	1	M6.25	2836	0.05 {0.04, 0.05}	−1.63 {−1.75, −1.49}	0.41	0.57	0.70
J04230607	(1)	Taurus	1	M6	2858	0.06 {0.05, 0.09}	−1.57 {−1.69, −1.24}	2.20	3.09	3.78
J04262939	(1)	Taurus	1	M6	2858	0.06 {0.05, 0.09}	−1.57 {−1.69, −1.24}	2.00	2.81	3.43
J04381486	(1)	Taurus	1	M7.25	2747	0.04 {0.03, 0.04}	−1.88 {−2.02, −1.75}	0.63	0.86	1.05
J04382134	(1)	Taurus	1	M6.5	2814	0.05 {0.04, 0.06}	−1.69 {−1.81, −1.57}	1.12	1.57	1.92
J04390163	(1)	Taurus	1	M6	2858	0.06 {0.05, 0.09}	−1.57 {−1.69, −1.24}	0.48	0.67	0.83
J04390396	(1)	Taurus	1	M7.25	2747	0.04 {0.03, 0.04}	−1.88 {−2.02, −1.75}	1.13	1.56	1.90
J04400067	(1)	Taurus	1	M6	2858	0.06 {0.05, 0.09}	−1.57 {−1.69, −1.24}	3.61	5.06	6.19
J04414825	(1)	Taurus	1	M7.75	2696	0.03 {0.02, 0.04}	−2.02 {−2.15, −1.88}	1.73	2.36	2.88

References. (1) This study; (2) Andrews et al. (2013); (3) Testi et al. (2016); (4) Barenfeld et al. (2016); (5) van der Plas et al. (2016); (6) Mathews et al. (2012). [UL] denotes upper limits calculated from submillimeter/mm nondetection.

(This table is available in its entirety in machine-readable form.)
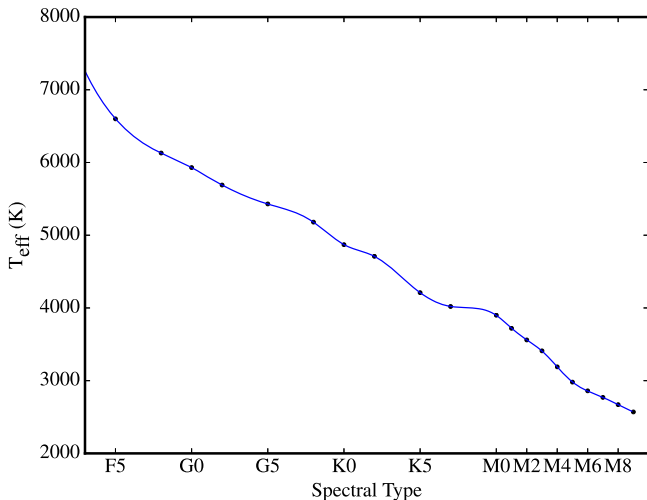
Figure 16. Correspondence between spectral type and effective temperature as provided in Herczeg & Hillenbrand (2014). A least-squared univariate spline interpolation (blue line) is used to provide fractional subclasses of spectral types.

Figure 17. Interpolation over mass and effective temperature as provided in the 1 Myr Baraffe et al. (1998) models.

dust temperature, which is used for the calculation of disk dust mass.

The resulting masses for all Taurus members with submillimeter detections were compared with the masses reported for Class II members in the SMA dish survey that formed the higher-mass comparison sample (Andrews et al. 2013). The approach to estimating masses in the SMA study applied Bayesian inference techniques from Jørgensen & Lindegren (2005) and Gennaro et al. (2012), first treating stellar luminosity and A_v as free parameters in fits of template stellar photosphere models to optical/NIR SEDs and then evaluating a corresponding conditional likelihood function to best-fit stellar masses and ages from three suites of pre-main-sequence stellar evolution grids (D'Antona & Mazzitelli 1997; Baraffe et al. 1998; Siess et al. 2000). For consistency, the values reported from the Baraffe et al. (1998) grid in Andrews et al. (2013) are used as comparison values for the results in this appendix.

The comparison with the literature masses and mass estimated from the spectral type, age of 1 Myr, and Baraffe

et al. (1998) grid is given in Figure 21 to consider the effect of using different approaches. The differences are negligible for objects fit with an age of 1 Myr within $\pm 0.1\,M_\odot$ (comparable to the range from ± 0.5 uncertainty in spectral type) for masses $\leqslant 1\,M_\odot$ and show a larger scatter of $\pm 0.3\,M_\odot$ for the higher-mass objects. Figure 22 shows the Taurus masses used in this study compared to the SMA survey, and the larger, systematic difference is dominated by the adoption of the newer model grid, following the trend shown in Figure 18. To understand whether the departure between older and newer vintages of the evolutionary model grids followed a systematic trend with the estimated ages of the targets from Andrews et al. (2013), the estimated stellar mass comparisons are also shown color-coded with the ages from the Bayesian inference approach in Figures 23 and 24. While Taurus members with older assigned ages from Andrews et al. (2013) show a more significant departure from the 1:1 relation, as to be expected, the difference in model grids remains the dominant factor. A similar comparison was performed for the Upper Sco population from Barenfeld et al. (2016) in Figure 25, demonstrating a similar significant impact of stellar model
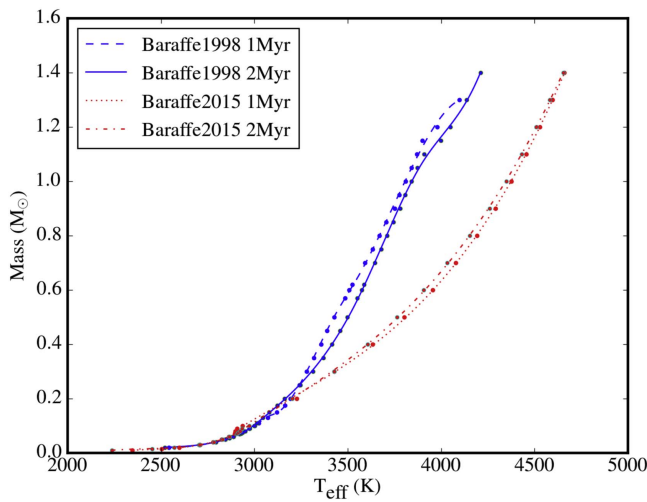
Figure 18. Interpolation over mass and effective temperature for each of the 1 and 2 Myr models provided by Baraffe et al. (1998, 2015).
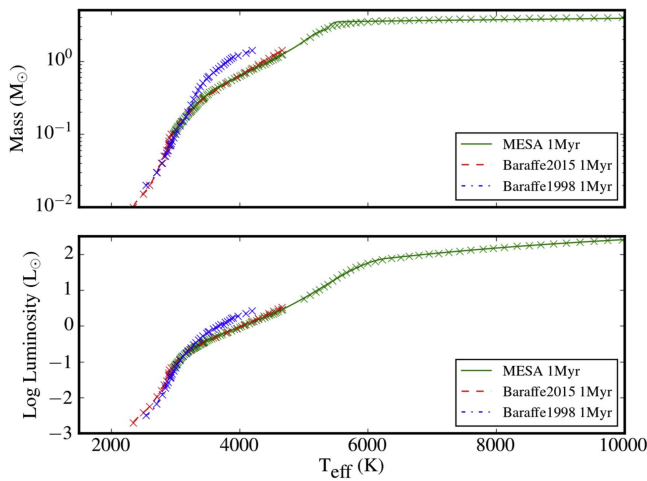

Figure 19. Interpolation over mass and effective temperature for the 1 Myr models provided by Baraffe et al. (1998, 2015) and from the MESA-based grid of MIST models (Choi et al. 2016), adopted for the derivation of central object mass for stars with temperatures corresponding to masses greater than 1.4 $M_\odot$.
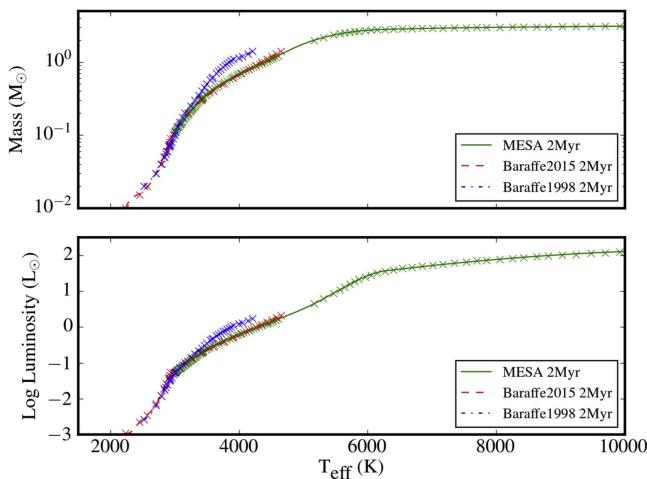

Figure 20. Interpolation over mass and effective temperature for the 2 Myr models provided by Baraffe et al. (1998, 2015) and from the MESA-based grid of MIST models (Choi et al. 2016), adopted for the derivation of central object mass for stars with temperatures corresponding to masses greater than 1.4 $M_\odot$.
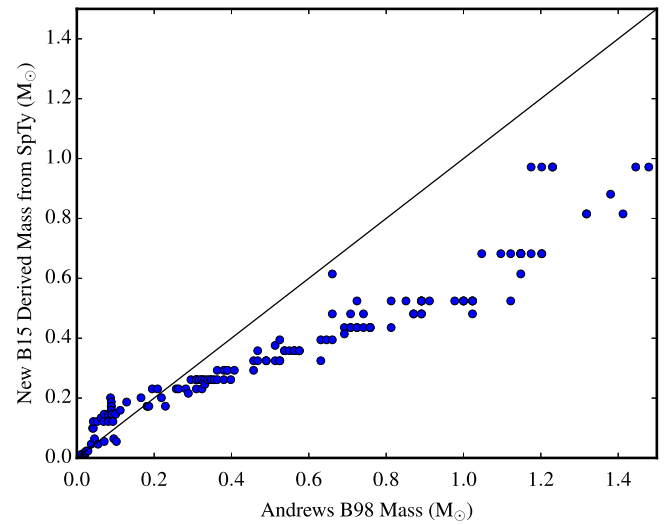
Figure 21. Comparison between the estimated stellar masses from Andrews et al. (2013) using the Baraffe et al. (1998) model grid and the newly derived masses using the approach described in this paper and the newer Baraffe et al. (2015) models.
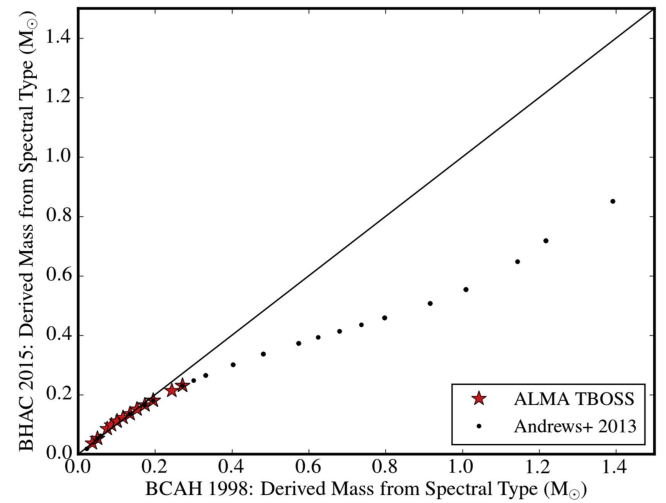
Figure 22. Comparison of stellar masses derived using the Baraffe et al. (1998) and Baraffe et al. (2015) models.
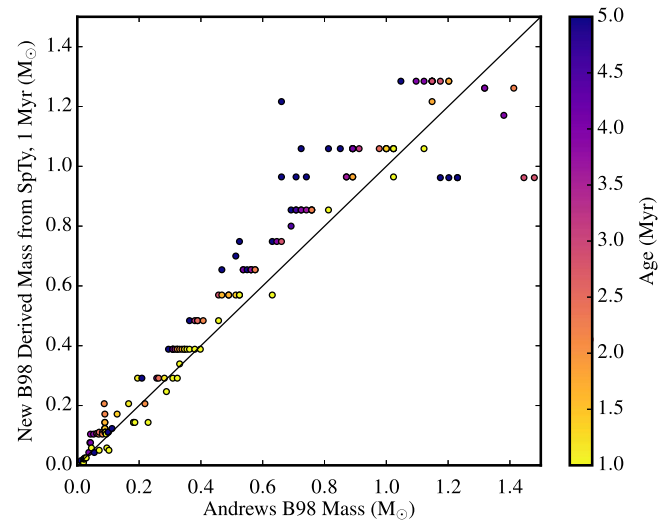
Figure 23. The 1 Myr comparison of the stellar masses derived using the approach described in this paper and the estimated stellar masses from Andrews et al. (2013), both using the Baraffe et al. (1998) evolutionary model grid. The color bar represents the derived age of the targets from the Bayesian analysis presented in Andrews et al. (2013).
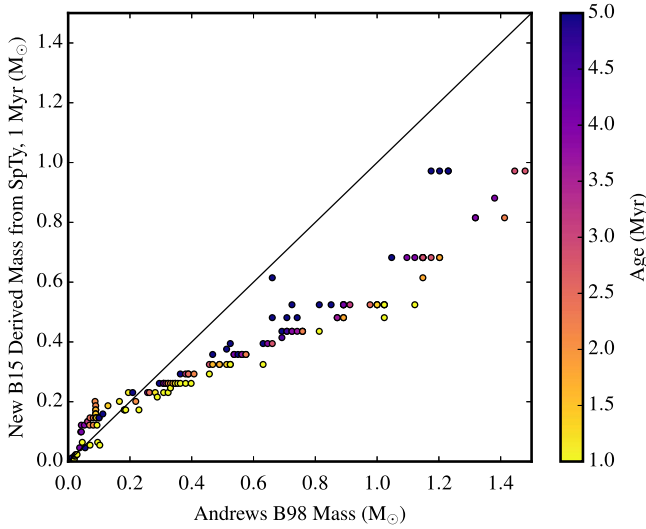
Figure 24. Same as Figure 21, underscoring the difference between the older and newer evolutionary grids. The points are color-coded to represent the derived age of the targets from the Bayesian analysis presented in Andrews et al. (2013).
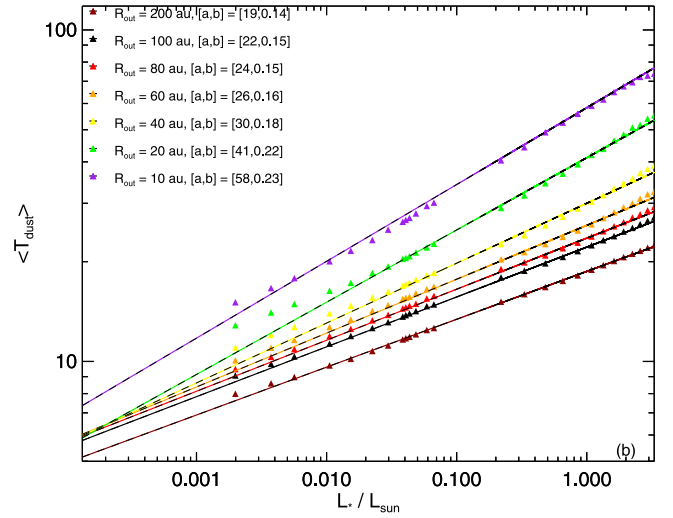
Figure 26. Dust temperature–luminosity scaling relations at 1 Myr adopted for targets in the Taurus star-forming region and used in the estimation of dust temperatures for our TBOSS targets and those in Andrews et al. (2013).
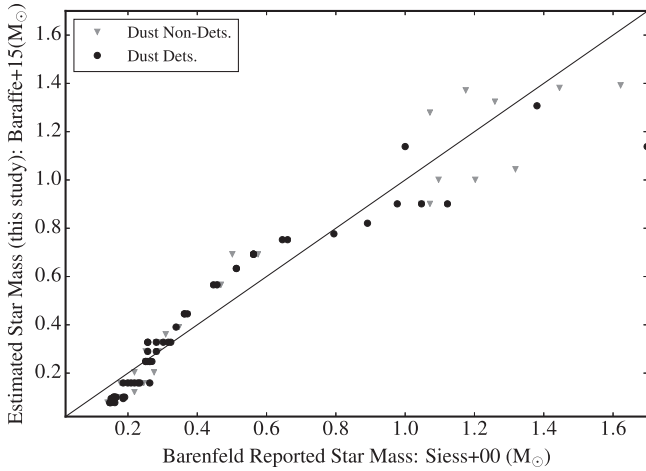
Figure 25. Comparison of the published stellar masses from Barenfeld et al. (2016) and the rederived stellar masses for the same population used in this work, applying the uniform method described in Section 6.3 and Appendix A.
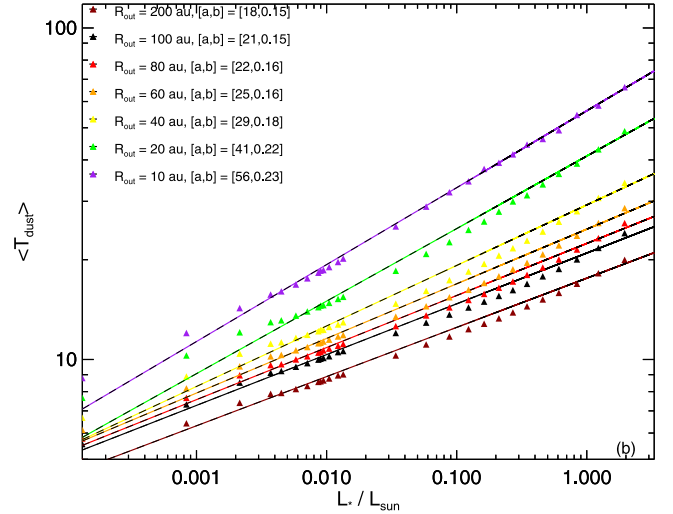
Figure 27. The 10 Myr scaling relations used to enable comparison between our targets and older star-forming regions; these relations were used for dust temperature estimation for targets in Upper Sco.

selection on estimated stellar mass, in this case between the Baraffe et al. (2015) models and the Siess et al. (2000) models.

Appendix B
Comparison of Estimated and Literature Dust Masses

As described in Section 6.1, the calculated disk dust mass is dependent upon the assumed dust temperature, T_{dust}, which in turn can be related to the central object luminosity, $L_{\odot}$, by the following prescription:

$$\langle T_{dust}\rangle = A(L_*/L_{\odot})^B \mathrm{K}. \qquad (4)$$

The power-law coefficients, A and B, are typically assumed to be 25 and 1/4, respectively, based upon stellar models of $L_* = 0.1$–$100\,L_{\odot}$ and assuming disks of radius 100 au. Revised procedures to generate the dust temperature–luminosity scaling relations for lower-mass central objects, described in detail in van der Plas et al. (2016), are outlined briefly here in their extension to the younger 1 Myr Taurus targets studied

in this work. Relations are derived from grids of disk models that vary the parameters of luminosity and disk outer radius while fixing scale height and profile, inclination, inner radius, surface density exponent, and disk mass ($\sim$1% of the (sub) stellar mass). Figure 26 shows the resulting power-law relation and coefficients for disks of different radii at 1 Myr, while Figure 27 shows the same relations for the 10 Myr objects. Power-law coefficients are provided for the range of disk radii explored from 10 to 200 au.

Following the approach outlined in Section 6.1, we then use the adopted dust temperatures from the revised power-law relations to infer the disk mass in submillimeter-sized grains using the flux density, dust opacity, and distance to the targets. To provide a uniform comparison with previous literature studies of disk-bearing objects in Upper Sco and ρ Ophiuchus, we also recalculated the dust masses for objects from previous studies using the same approach. Reported fluxes and spectral types from the previous surveys were used to reestimate the
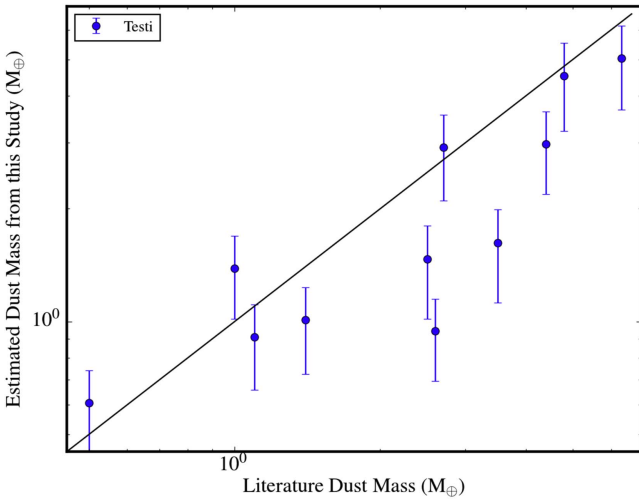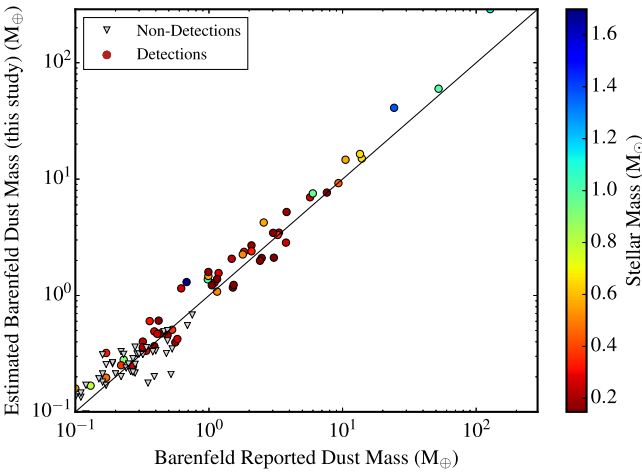
Figure 28. Comparison of dust mass measurements for a sample of objects from ρ Ophiuchus from Testi et al. (2016) and the uniform method of dust mass calculation presented in this study.
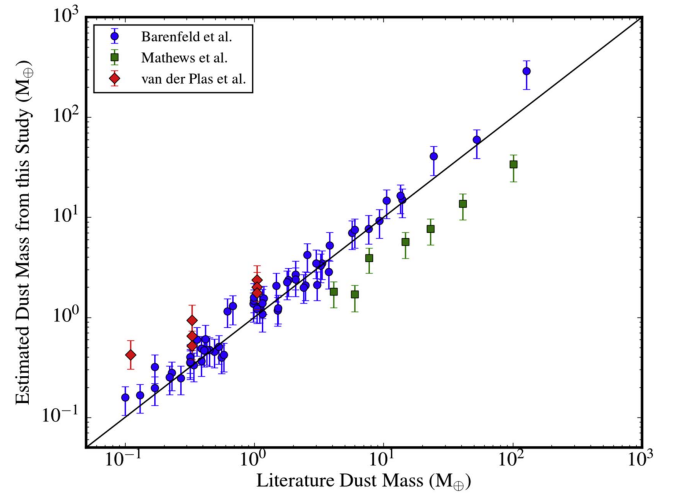
Figure 30. Dust mass measurements for the combined sample of Upper Sco objects from Mathews et al. (2012), Barenfeld et al. (2016), and van der Plas et al. (2016) compared with the rederived masses using the uniform method of dust mass calculation presented in this study.

For the Upper Sco population, the literature and reestimated dust mass comparison is shown for the Barenfeld et al. (2016) detections and upper limits in Figure 29 and for the combined Upper Sco populations in Figure 30. The literature dust masses and rederived dust mass values using the approach described in this work are in close agreement, with no strong dependence on stellar mass, emphasizing the dependence of M_{dust}–M_* relations on the choice of stellar model, as illustrated in Appendix A. The previous literature measurements and the rederived dust masses from the uniform approach in this study agree at the 11% level across all three Upper Sco surveys, with the higher-mass objects from Mathews et al. (2012) systematically higher and the van der Plas et al. (2016) population systematically lower. Offsets for the lowest- and highest-mass members presented in van der Plas et al. (2016) and Mathews et al. (2012) may be explained by reporting of masses derived from radiative transfer modeling, similar to the differences between the analytic approach and model-estimated masses seen in this study (Section 6.2). The dust mass values recalculated in this work for each previous literature study are given in full in Table 14.

Figure 29. Comparison of the published Upper Sco dust masses from Barenfeld et al. (2016) and the dust masses rederived for the same population using the uniform method of dust mass calculation presented in this study.

stellar parameters of T_{eff} and $L_\odot$ (as described in Appendix A) using the Baraffe et al. (2015) evolutionary models. The revised 1 Myr luminosity–dust temperature relations were applied to the ρ Oph population from Testi et al. (2016), while the 10 Myr relations were applied to the Upper Sco population from Mathews et al. (2012), Barenfeld et al. (2016), and van der Plas et al. (2016). For the ρ Oph population, the literature values are plotted against the new dust mass estimates in Figure 28, which show agreement at the 20% level, with systematically higher previously published values.

Appendix C
MCFOST Results

This appendix provides the SEDs for the targets within our survey overlaid with the resulting best-fit MCFOST models, as described in Section 6.2. Data and fits are shown for stellar hosts in Figure 31 and for brown dwarfs in Figure 32.
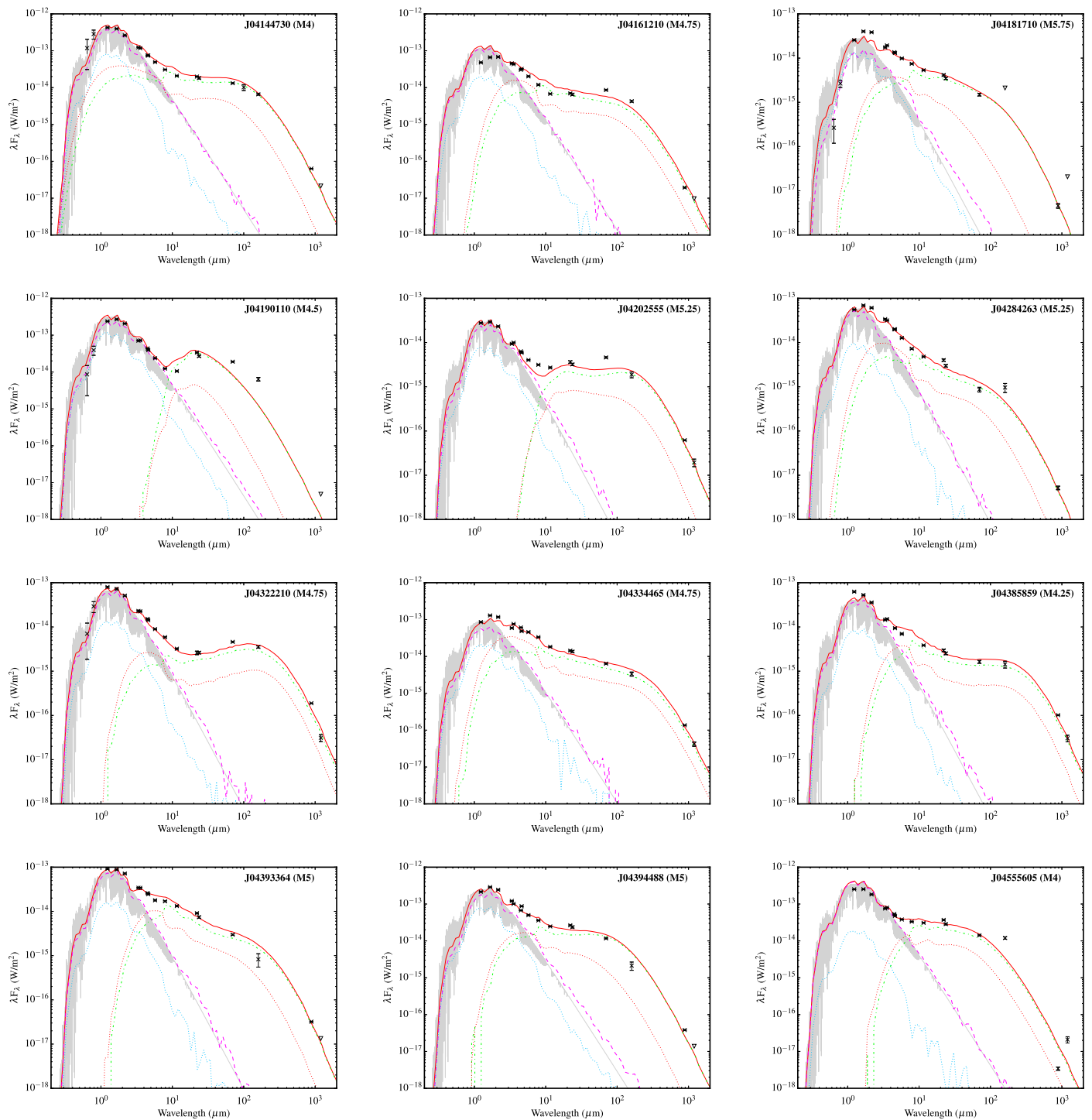
Figure 31. SEDs with best-fit models from MCFOST for the stellar targets within this survey (M4–M5.75) in order of increasing right ascension. Fluxes as a function of wavelength (μm; black symbols) are compiled from Bulger et al. (2014) with the new 885 μm measurements from this study, and upper limits are denoted with downward-pointing triangles where applicable. In addition to the dereddened stellar photosphere (gray regions) and best-fit full SED (red solid line), the contributing disk components are given by the following lines: scattered light (blue dotted), direct starlight (magenta dashed), thermal emission (red dotted), and scattered thermal emission (green dot-dashed).
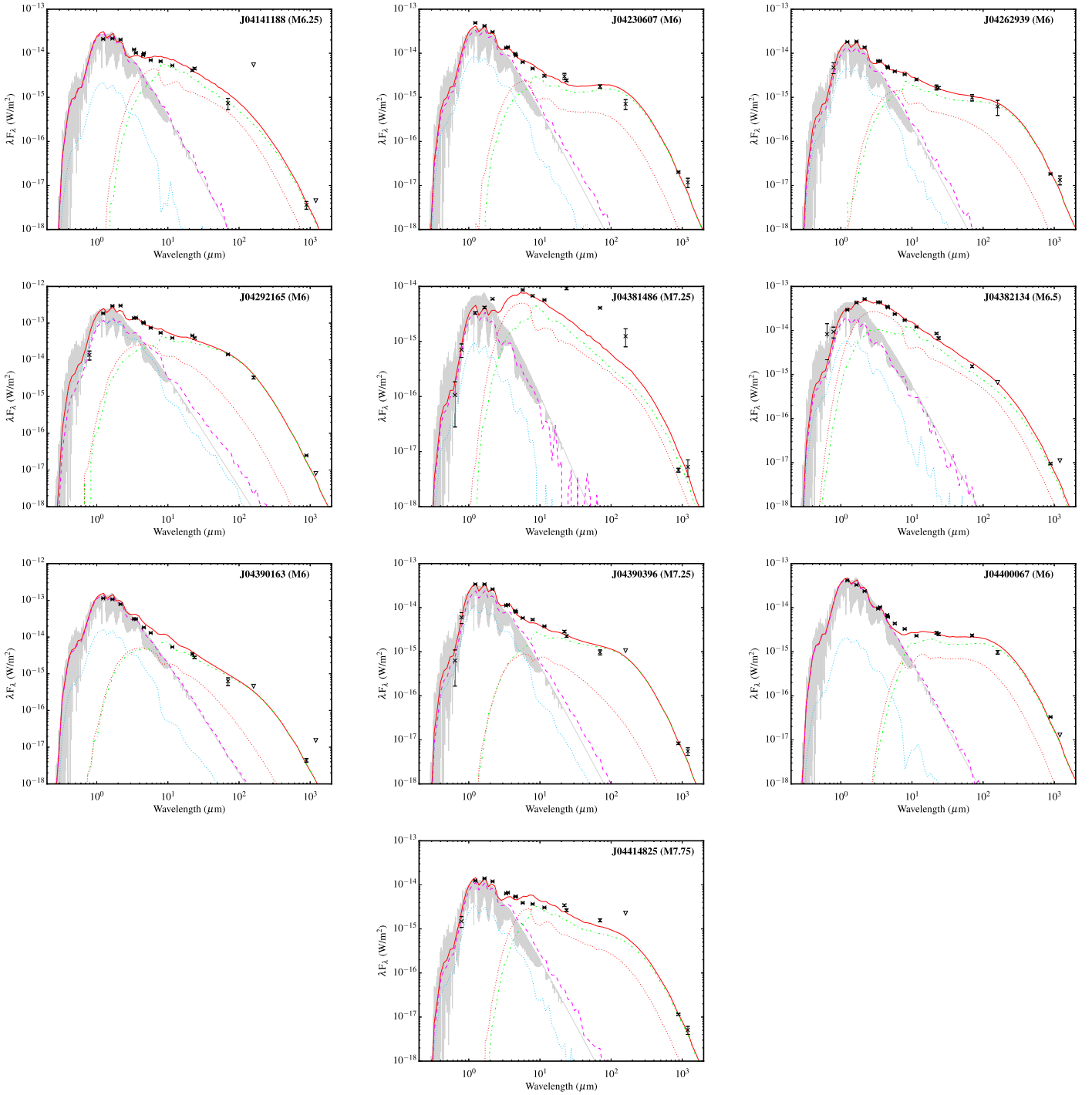
Figure 32. SEDs with best-fit models from MCFOST for the substellar targets within this survey (M6 and later) in order of increasing right ascension. Symbols and lines are the same as in Figure 31.

Appendix D
Table of Stellar Parameters and Disk Dust Masses
## from a Uniform Approach

In this appendix, we provide the full set of stellar parameters and associated disk dust masses for the star-forming regions described in this paper, applying the uniform methodology described in Appendices A and B. These results are summarized in Table 14. In Table 15, we provide the full table of analytic dust masses for the TBOSS ALMA sample, corresponding to dust temperatures for disks of radii ranging from 10 to 200 au.

Table 15
Dust Masses

| Target | $T_{dust} = 25(L_*/L_\odot)^{0.25}$ | | $R = 10$ au | | $R = 20$ au | | $R = 40$ au | | $R = 60$ au | | $R = 80$ au | | $R = 100$ au | | $R = 200$ au | |
	T_{dust}(K)	M_{dust}(⊕)	T_d(K)	M_d(⊕)	T_d(K)	M_d(⊕)	T_d(K)	M_d(⊕)	T_d(K)	M_d(⊕)	T_d(K)	M_d(⊕)	T_d(K)	M_d(⊕)	T_d(K)	M_d(⊕)
J04292165	10.1	5.92	25.3	1.35	18.5	2.10	15.68	2.72	14.6	3.05	14.0	3.29	12.8	3.82	11.5	4.67
J04141188	9.8	0.92	24.5	0.20	18.0	0.32	15.28	0.41	14.3	0.46	13.7	0.49	12.5	0.57	11.2	0.70
J04230607	10.1	4.78	25.3	1.09	18.5	1.69	15.68	2.20	14.6	2.47	14.0	2.66	12.8	3.09	11.5	3.78
J04262939	10.1	4.35	25.3	0.99	18.5	1.54	15.68	2.00	14.6	2.24	14.0	2.42	12.8	2.81	11.5	3.43
J04381486	8.5	1.61	21.4	0.31	15.8	0.50	13.76	0.62	13.0	0.69	12.5	0.74	11.5	0.86	10.4	1.05
J04382134	9.5	2.61	23.7	0.56	17.4	0.88	14.90	1.13	14.0	1.26	13.4	1.35	12.3	1.57	11.0	1.92
J04390163	10.1	1.05	25.3	0.24	18.5	0.37	15.68	0.48	14.6	0.54	14.0	0.58	12.8	0.68	11.5	0.83
J04390396	8.5	2.91	21.4	0.57	15.8	0.90	13.76	1.13	13.0	1.25	12.5	1.33	11.5	1.56	10.4	1.90
J04400067	10.1	7.85	25.3	1.78	18.5	2.78	15.68	3.61	14.6	4.05	14.0	4.36	12.8	5.06	11.5	6.19
J04414825	7.8	4.86	19.9	0.88	14.7	1.40	12.99	1.73	12.4	1.89	11.9	2.01	11.0	2.37	9.9	2.88
J04144730	16.7	6.26	40.0	1.90	28.7	2.89	22.43	4.04	20.1	4.73	18.8	5.20	17.3	5.94	15.2	7.30
J04161210	14.4	2.43	34.9	0.69	25.2	1.05	20.16	1.44	18.3	1.67	17.2	1.82	15.8	2.09	13.9	2.56
J04181710	10.6	0.99	26.4	0.23	19.3	0.36	16.19	0.47	15.0	0.53	14.4	0.58	13.2	0.67	11.8	0.82
J04202555	12.9	9.40	31.6	2.51	22.9	3.85	18.63	5.18	17.0	5.95	16.1	6.47	14.8	7.45	13.1	9.13
J04284263	12.9	0.79	31.6	0.21	22.9	0.32	18.63	0.43	17.0	0.50	16.1	0.54	14.8	0.62	13.1	0.76
J04322210	14.4	23.69	34.9	6.71	25.2	10.24	20.16	14.02	18.3	16.24	17.2	17.74	15.8	20.35	13.9	24.98
J04334465	14.4	17.13	34.9	4.85	25.2	7.40	20.16	10.14	18.3	11.75	17.2	12.83	15.8	14.72	13.9	18.07
J04385859	16.0	10.77	38.4	3.21	27.7	4.88	21.74	6.78	19.5	7.92	18.3	8.69	16.8	9.93	14.8	12.21
J04393364	13.6	4.43	33.1	1.22	24.0	1.86	19.36	2.53	17.6	2.92	16.7	3.18	15.3	3.65	13.5	4.48
J04394488	13.6	5.27	33.1	1.45	24.0	2.22	19.36	3.01	17.6	3.47	16.7	3.78	15.3	4.35	13.5	5.33
J04555605	16.7	0.34	40.0	0.10	28.7	0.16	22.43	0.22	20.1	0.26	18.8	0.28	17.3	0.32	15.2	0.39
J05075496	16.7	0.96	40.0	0.29	28.7	0.45	22.43	0.62	20.1	0.73	18.8	0.80	17.3	0.92	15.2	1.13

ORCID iDs

K. Ward-Duong https://orcid.org/0000-0002-4479-8291
J. Bulger https://orcid.org/0000-0003-4641-2003
G. van der Plas https://orcid.org/0000-0001-5688-187X
C. Pinte https://orcid.org/0000-0001-5907-5179
A. P. Jackson https://orcid.org/0000-0003-4393-9520
N. J. Turner https://orcid.org/0000-0001-8292-1943
P. Harvey https://orcid.org/0000-0003-3334-9463
A. Hales https://orcid.org/0000-0001-5073-2849
R. J. De Rosa https://orcid.org/0000-0002-4918-0247

References

Alibert, Y., Mordasini, C., Benz, W., & Winisdoerffer, C. 2005, A&A, 434, 343
Andrews, S. M., Rosenfeld, K. A., Kraus, A. L., & Wilner, D. J. 2013, ApJ, 771, 129
Andrews, S. M., & Williams, J. P. 2005, ApJ, 631, 1134
Andrews, S. M., & Williams, J. P. 2007, ApJ, 659, 705
Anglada-Escudé, G., Amado, P. J., Barnes, J., et al. 2016, Natur, 536, 437
Ansdell, M., Williams, J. P., Manara, C. F., et al. 2017, AJ, 153, 240
Ansdell, M., Williams, J. P., van der Marel, N., et al. 2016, ApJ, 828, 46
Baraffe, I., Chabrier, G., Allard, F., & Hauschildt, P. H. 1998, A&A, 337, 403
Baraffe, I., Homeier, D., Allard, F., & Chabrier, G. 2015, A&A, 577, A42
Barenfeld, S. A., Carpenter, J. M., Ricci, L., & Isella, A. 2016, ApJ, 827, 142
Beckwith, S. V. W., Sargent, A. I., Chini, R. S., & Guesten, R. 1990, AJ, 99, 924
Bertout, C., Robichon, N., & Arenou, F. 1999, A&A, 352, 574
Birnstiel, T., Dullemond, C. P., & Brauer, F. 2010, A&A, 513, A79
Blaauw, A. 1978, in Internal Motions and Age of the Sub-Association Upper Scorpio, ed. L. V. Mirzoyan (Yerevan: Publishing House of the Armenian Academy of Sciences), 101
Boss, A. P. 1997, Sci, 276, 1836
Bouvier, A., & Wadhwa, M. 2010, NatGe, 3, 637
Bouy, H., Huélamo, N., Pinte, C., et al. 2008, A&A, 486, 877
Bowler, B. P. 2016, PASP, 128, 102001
Bowler, B. P., Liu, M. C., Shkolnik, E. L., & Tamura, M. 2015, ApJS, 216, 7
Briceño, C., Luhman, K. L., Hartmann, L., Stauffer, J. R., & Kirkpatrick, J. D. 2002, ApJ, 580, 317
Bulger, J., Patience, J., Ward-Duong, K., et al. 2014, A&A, 570, A29
Carpenter, J. M., Mamajek, E. E., Hillenbrand, L. A., & Meyer, M. R. 2006, ApJL, 651, L49
Carpenter, J. M., Ricci, L., & Isella, A. 2014, ApJ, 787, 42
Chambers, J. 2010, in Exoplanets, Terrestrial Planet Formation, ed. S. Seager (Tucson, AZ: Univ. Arizona Press), 297
Chambers, J. E., & Wetherill, G. W. 1998, Icar, 136, 304
Chauvin, G., Lagrange, A.-M., Dumas, C., et al. 2004, A&A, 425, L29
Choi, J., Dotter, A., Conroy, C., et al. 2016, ApJ, 823, 102
Cieza, L. A., Schreiber, M. R., Romero, G. A., et al. 2012, ApJ, 750, 157
Clanton, C., & Gaudi, B. S. 2014, ApJ, 791, 91
Connelly, J. N., Amelin, Y., Krot, A. N., & Bizzarro, M. 2008, ApJL, 675, L121
Connelly, J. N., Bizzarro, M., Krot, A. N., et al. 2012, Sci, 338, 651
Cumming, A., Butler, R. P., Marcy, G. W., et al. 2008, PASP, 120, 531
Currie, T., & Sicilia-Aguilar, A. 2011, ApJ, 732, 24
Daemgen, S., Bonavita, M., Jayawardhana, R., Lafrenière, D., & Janson, M. 2015, ApJ, 799, 155
D'Antona, F., & Mazzitelli, I. 1997, MmSAI, 68, 807
Dauphas, N., & Pourmand, A. 2011, Natur, 473, 489
Dittmann, J. A., Irwin, J. M., Charbonneau, D., et al. 2017, Natur, 544, 333
Dobashi, K., Uehara, H., Kandori, R., et al. 2005, PASJ, 57, S1
Dullemond, C. P., & Dominik, C. 2005, A&A, 434, 971
Eisner, J. A., Bally, J. M., Ginsburg, A., & Sheehan, P. D. 2016, ApJ, 826, 16
Gaidos, E. 2017, MNRAS, 470, L1
Gennaro, M., Prada Moroni, P. G., & Tognelli, E. 2012, MNRAS, 420, 986
Gillon, M., Triaud, A. H. M. J., Demory, B.-O., et al. 2017, Natur, 542, 456
Guieu, S., Dougados, C., Monin, J.-L., Magnier, E., & Martín, E. L. 2006, A&A, 446, 485
Helled, R., Anderson, J. D., Podolak, M., & Schubert, G. 2011, ApJ, 726, 15
Henry, T. J., Jao, W.-C., Subasavage, J. P., et al. 2006, AJ, 132, 2360
Herczeg, G. J., & Hillenbrand, L. A. 2014, ApJ, 786, 97

Hildebrand, R. H. 1983, QJRAS, 24, 267
Itoh, Y., Tamura, M., & Nakajima, T. 1999, AJ, 117, 1471
Johansen, A., & Youdin, A. 2007, ApJ, 662, 627
Johnson, J. A., Clanton, C., Howard, A. W., et al. 2011, ApJS, 197, 26
Jørgensen, B. R., & Lindegren, L. 2005, A&A, 436, 127
Kelly, B. C. 2007, ApJ, 665, 1489
Kenyon, S. J., Dobrzycka, D., & Hartmann, L. 1994, AJ, 108, 1872
Kenyon, S. J., & Hartmann, L. 1995, ApJS, 101, 117
Konopacky, Q. M., Ghez, A. M., Rice, E. L., & Duchêne, G. 2007, ApJ, 663, 394
Kraus, A. L., & Hillenbrand, L. A. 2007, ApJ, 662, 413
Kraus, A. L., & Hillenbrand, L. A. 2009, ApJ, 704, 531
Kraus, A. L., Ireland, M. J., Hillenbrand, L. A., & Martinache, F. 2012, ApJ, 745, 19
Lambrechts, M., & Johansen, A. 2012, A&A, 544, A32
Lee, N., Williams, J. P., & Cieza, L. A. 2011, ApJ, 736, 135
Lépine, S. 2005, AJ, 130, 1247
Levison, H. F., Kretke, K. A., & Duncan, M. J. 2015a, Natur, 524, 322
Levison, H. F., Kretke, K. A., Walsh, K. J., & Bottke, W. F. 2015b, PNAS, 112, 14180
Lodders, K. 2003, ApJ, 591, 1220
Luhman, K. L. 2004, ApJ, 617, 1216
Luhman, K. L., Allen, P. R., Espaillat, C., Hartmann, L., & Calvet, N. 2010, ApJS, 186, 111
Luhman, K. L., Lada, C. J., Hartmann, L., et al. 2005, ApJL, 631, L69
Luhman, K. L., Mamajek, E. E., Allen, P. R., & Cruz, K. L. 2009, ApJ, 703, 399
Luhman, K. L., & Rieke, G. H. 1996, ApJ, 461, 298
Luhman, K. L., Stauffer, J. R., Muench, A. A., et al. 2003, ApJ, 593, 1093
Luhman, K. L., Whitney, B. A., Meade, M. R., et al. 2006, ApJ, 647, 1180
MacPherson, G. J., Davis, A. M., & Zinner, E. K. 1995, Metic, 30, 365
Martín, E. L., Dougados, C., Magnier, E., et al. 2001, ApJL, 561, L195
Mathews, G. S., Pinte, C., Duchêne, G., Williams, J. P., & Ménard, F. 2013, A&A, 558, A66
Mathews, G. S., Williams, J. P., Ménard, F., et al. 2012, ApJ, 745, 23
McMullin, J. P., Waters, B., Schiebel, D., Young, W., & Golap, K. 2007, in ASP Conf. Ser. 376, Astronomical Data Analysis Software and Systems XVI, ed. R. A. Shaw, F. Hill, & D. J. Bell (San Francisco, CA: ASP), 127
Mulders, G. D., Pascucci, I., & Apai, D. 2015, ApJ, 814, 130
Pascucci, I., Testi, L., Herczeg, G. J., et al. 2016, ApJ, 831, 125
Pecaut, M. J., & Mamajek, E. E. 2013, ApJS, 208, 9
Pecaut, M. J., Mamajek, E. E., & Bubar, E. J. 2012, ApJ, 746, 154
Pérez, L. M., Chandler, C. J., Isella, A., et al. 2015, ApJ, 813, 41
Petry, D., Vila-Vilaro, B., Villard, E., Komugi, S., & Schnee, S. 2014, Proc. SPIE, 9152, 91520J
Pinte, C., Harries, T. J., Min, M., et al. 2009, A&A, 498, 967
Pinte, C., Ménard, F., Duchêne, G., & Bastien, P. 2006, A&A, 459, 797
Poglitsch, A., Waelkens, C., Geis, N., et al. 2010, A&A, 518, L2
Pollack, J. B., Hubickyj, O., Bodenheimer, P., et al. 1996, Icar, 124, 62
Ricci, L., Testi, L., Natta, A., et al. 2010, A&A, 512, A15
Ricci, L., Testi, L., Natta, A., et al. 2014, ApJ, 791, 20
Robitaille, T., & Bressert, E. 2012, APLpy: Astronomical Plotting Library in Python, Astrophysics Source Code Library, ascl:1208.017
Russell, S. S., Hartmann, L., Cuzzi, J., et al. 2006, in Meteorites and the Early Solar System II, Timescales of the Solar Protoplanetary Disk, ed. D. S. Lauretta & H. Y. McSween (Tucson, AZ: Univ. Arizona Press), 233
Schlieder, J. E., Beichman, C. A., Meyer, M. R., & Greene, T. 2016, in IAU Symp. 314, Young Stars & Planets Near the Sun, ed. J. H. Sun, B. Kastner, & S. A. Stelzer (Cambridge: Cambridge Univ. Press), 288
Scholz, A., Jayawardhana, R., & Wood, K. 2006, ApJ, 645, 1498
Siess, L., Dufour, E., & Forestini, M. 2000, A&A, 358, 593
Slesnick, C. L., Carpenter, J. M., Hillenbrand, L. A., & Mamajek, E. E. 2006, AJ, 132, 2665
Testi, L., Natta, A., Scholz, A., et al. 2016, A&A, 593, A111
Todorov, K., Luhman, K. L., & McLeod, K. K. 2010, ApJL, 714, L84
Torres, R. M., Loinard, L., Mioduszewski, A. J., & Rodríguez, L. F. 2009, ApJ, 698, 242
van der Plas, G., Ménard, F., Ward-Duong, K., et al. 2016, ApJ, 819, 102
Weidenschilling, S. J. 1977, Ap&SS, 51, 153
White, R. J., & Basri, G. 2003, ApJ, 582, 1109
Williams, J. P., Cieza, L. A., Andrews, S. M., et al. 2013, MNRAS, 435, 1671
Youdin, A., & Johansen, A. 2007, ApJ, 662, 613
Youdin, A. N., & Goodman, J. 2005, ApJ, 620, 459
Zacharias, N., Finch, C., Subasavage, J., et al. 2015, AJ, 150, 101